Supplementary Information

Ligand Environment Engineering of Nickel Single Atomic Sites for Efficient Electrochemical Carbon Dioxide Reduction Reaction

Min Sung Kim,‡[ab] Adyasa Priyadarsini,‡[c] Ju-Hyeon Lee,[ab] Jin-Gyu Bae,[ab] Jeong Yeon Heo,[ab] Hyeon Jeong Lee,[d] Shyam Kattel,*[e] and Ji Hoon Lee,*[ab]*

[a] School of Materials Science and Engineering, Kyungpook National University, Daegu 41566, Republic of Korea

[b] KNU Advanced Material Research Institute, Kyungpook National University, Daegu 41566, Republic of Korea

[c] Department of Physics, Florida A&M University, Tallahassee, FL 32307, United States

[d] Department of Materials Science and Engineering, Ulsan National Institute of Science and Technology, Ulsan 44919, Republic of Korea

[e] Department of Physics, University of Central Florida, Orlando, FL 32816, United States

‡ These authors contributed equally to this work.

*Corresponding authors:

H. J. Lee (hyeonjeong.lee@unist.ac.kr)

S. Kattel (shyam.kattel@ucf.edu)

J. H. Lee (jihoonlee@knu.ac.kr)

Supplementary Figure Caption:

Fig. S1. The N_2 adsorption/desorption isotherms at 77K for Ni-SACs.

Fig. S2. Pore size distribution curves based on NLDFT method.

Fig. S3. The ESCA calculations for a series of Ni-SACs.

Fig. S4. High resolution TEM analyses of Ni-SACs.

Fig. S5. Raman spectra for a series of Ni-SACs.

Fig. S6. XANES characterization for a series of Ni-SACs.

Fig. S7. The integrated area of the **peak A** for the series of Ni-SACs.

Fig. S8. The integrated area of the **peak B** for the series of Ni-SACs.

Fig. S9. Integrated area values of a series of catalysts for (a) **peak A** and (b) **peak B**.

Fig. S10. EXAFS fitting profiles for Ni-SACs and Ni-Pc.

Fig. S11. High resolution N 1s spectra of the samples and correlation of the carbon with N contents.

Fig. S12. Faradaic efficiencies for CO and H_2 of the series of Ni-SACs at different potentials.

Fig. S13. Partial current densities for CO and H_2 of the series of Ni-SACs.

Fig. S14. Normalized partial current densities for CO and H_2 of the series of Ni-SACs.

Fig. S15. Electrochemical performance of Ni-SAC-700/H_2.

Fig. S16. Electrochemical performance of Ni-SAC-800/Ar.

Fig. S17. Electrochemical performance of Ni-SAC-800/H_2.

Fig. S18. Electrochemical performance of Ni-SAC-900/Ar.

Fig. S19. Electrochemical performance of Ni-SAC-900/H_2.

Fig. S20. Tafel plots for Ni-SACs.

Fig. S21. Correlation between J_{CO} and N coordination for a series of Ni-SACs.

Fig. S22. EIS analyses for series of Ni-SACs.

Fig. S23. Stability tests of Ni-SACs performed at –0.6 V_{RHE}.

Fig. S24. Photographs of step-by-step cell assembly for our flow cell reactor.

Suppulementary Table Caption:

Table S1. Elemental analysis results and electrode specifications of Ni-SAC catalysts.

Table S2. Structural model for EXAFS fitting in this study.

Table S3. The EXAFS fitting parameters and results for Ni-Pc.

Table S4. The EXAFS fitting parameters and results for Ni-SAC-700/H_2.

Table S5. The EXAFS fitting parameters and results for Ni-SAC-800/Ar.

Table S6. The EXAFS fitting parameters and results for Ni-SAC-800/H_2.

Table S7. The EXAFS fitting parameters and results for Ni-SAC-900/Ar.

Table S8. The EXAFS fitting parameters and results for Ni-SAC-900/H_2.

Table S9. Bond length of Ni–N and Ni–C for the energetically optimized Ni-N_xC_y configurations.

Table S10. Bader charge analysis of Ni-SACs with different vacancy and N decoration.

Table S11. The limiting potential values calculated from the PDS of CO_2RR and HER processes.

Table S12. Bond length of Ni–N and Ni–C before and after intermediates adsorption.

Table S13. The d-band center (ε_d) and free energy change of *COOH and *H formation.

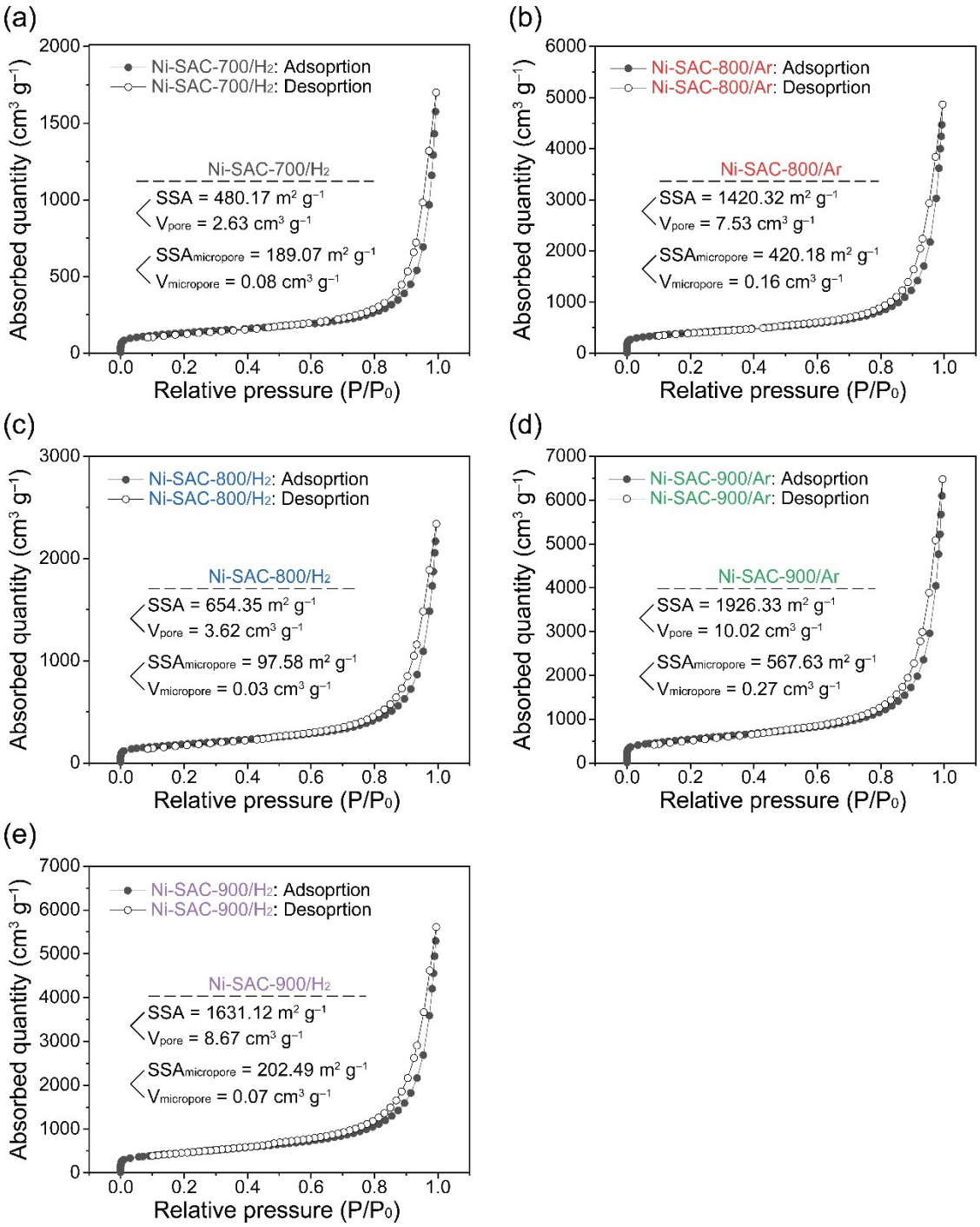

Fig. S1. N_2 adsorption/desorption isotherms at 77 K for (a) Ni-SAC-700/H_2, (b) Ni-SAC-800/Ar, (c) Ni-SAC-800/H_2, (d) Ni-SAC-900/Ar, and (e) Ni-SAC-900H_2.

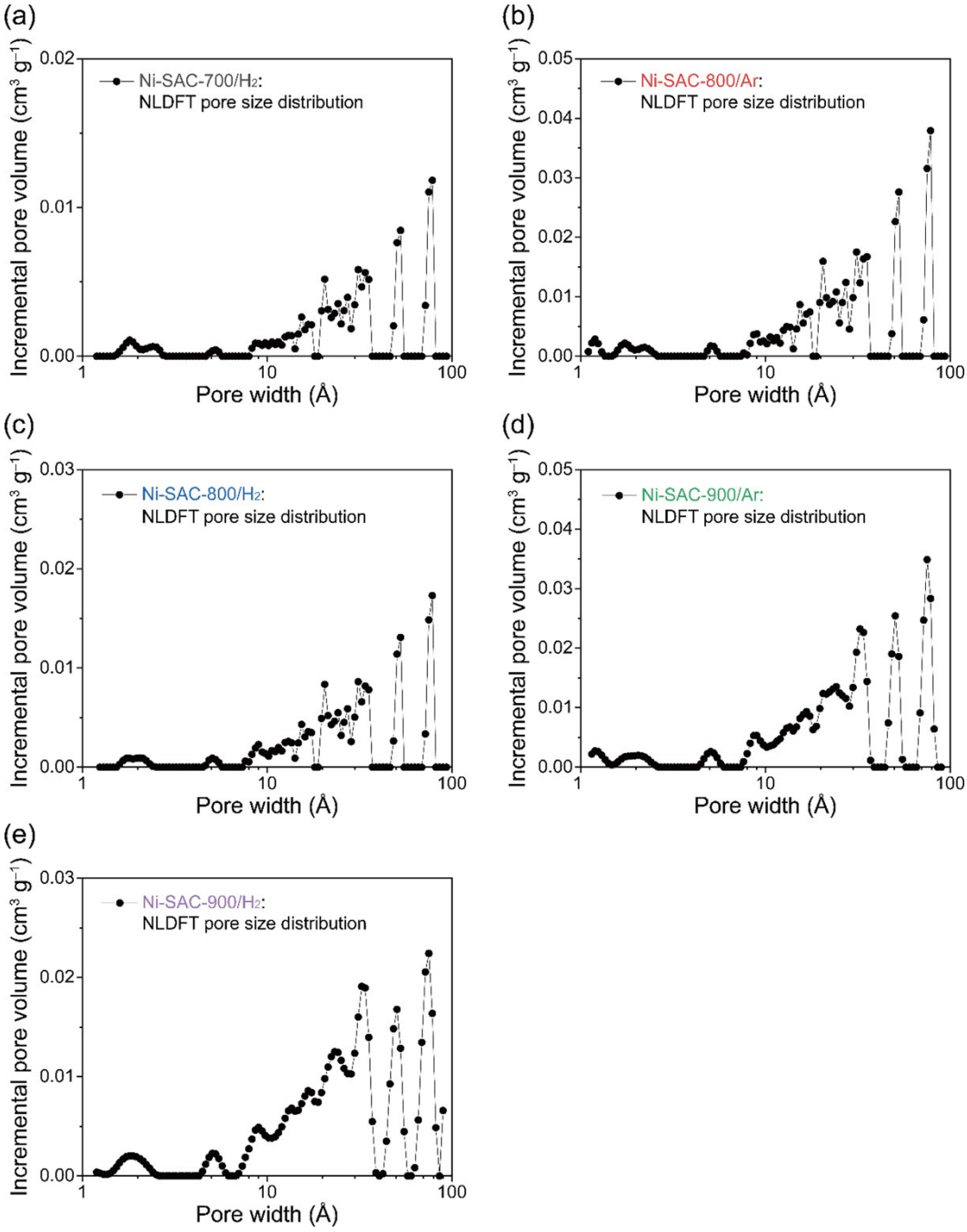

Fig. S2. Pore size distribution curves based on NLDFT method assuming slit-shaped pore geometry for (a) Ni-SAC-700/H_2, (b) Ni-SAC-800/Ar, (c) Ni-SAC-800/H_2, (d) Ni-SAC-900/Ar, and (e) Ni-SAC-900H_2.

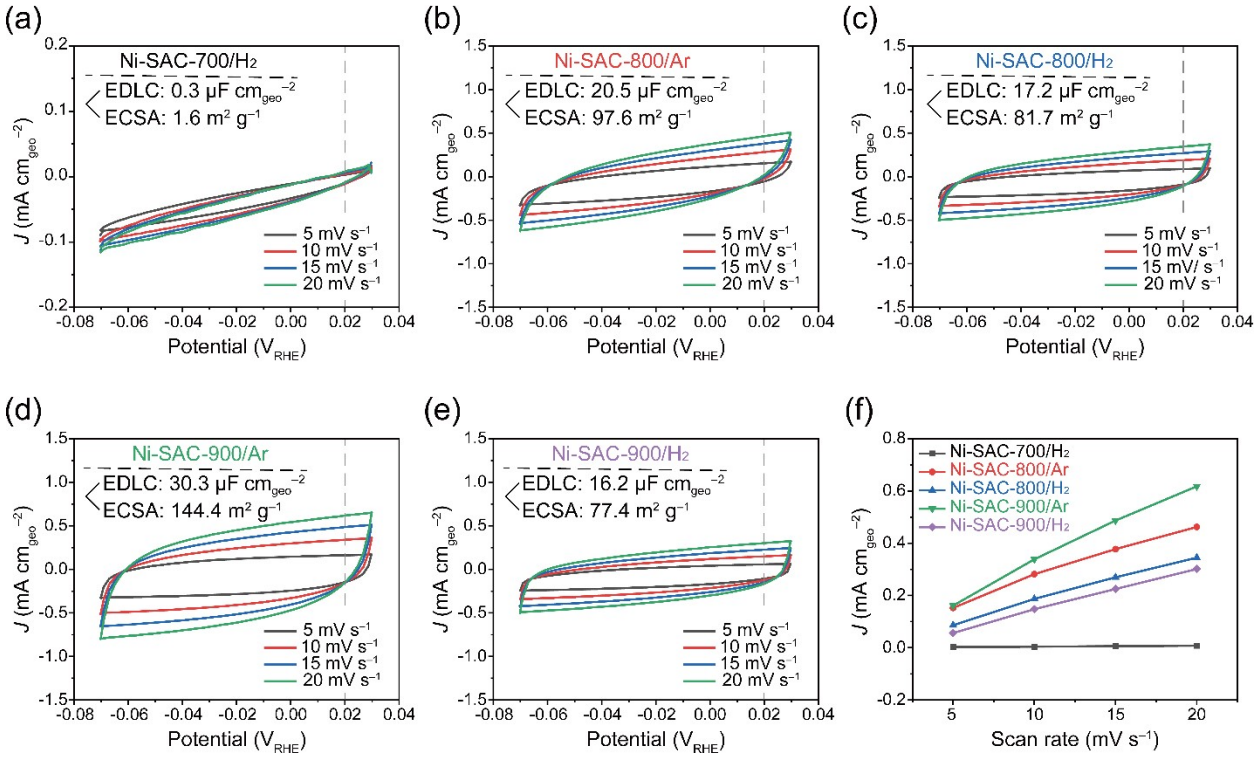

Fig. S3. The ESCA calculations for a series of Ni-SACs. (a-e) CV curves in 0.5M $KHCO_3$ electrolyte at different scan rates. (f) Calculated EDLC values from the slope in a plot of J versus scan rate. Assuming the double layer capacitance per cm^2 of the electrochemical surface area of the catalyst is identical to that of graphene, namely, 21 μF cm^{-2}.

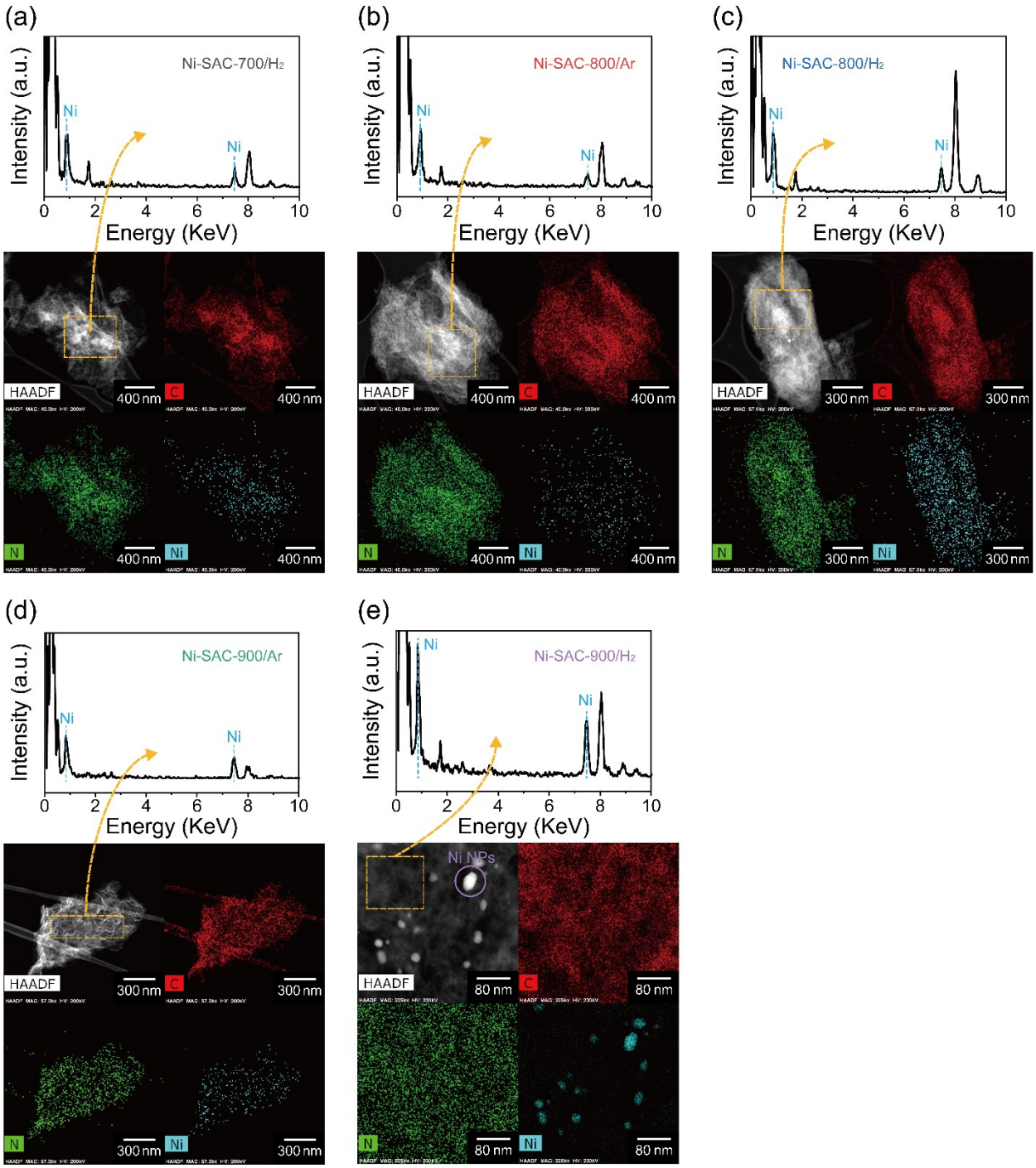

Fig. S4. High resolution TEM analyses of Ni-SACs. (a) Ni-SAC-700/H_2. (b) Ni-SAC-800/Ar. (c) Ni-SAC-800/H_2. (d) Ni-SAC-900/Ar. (e) Ni-SAC-900/H_2.

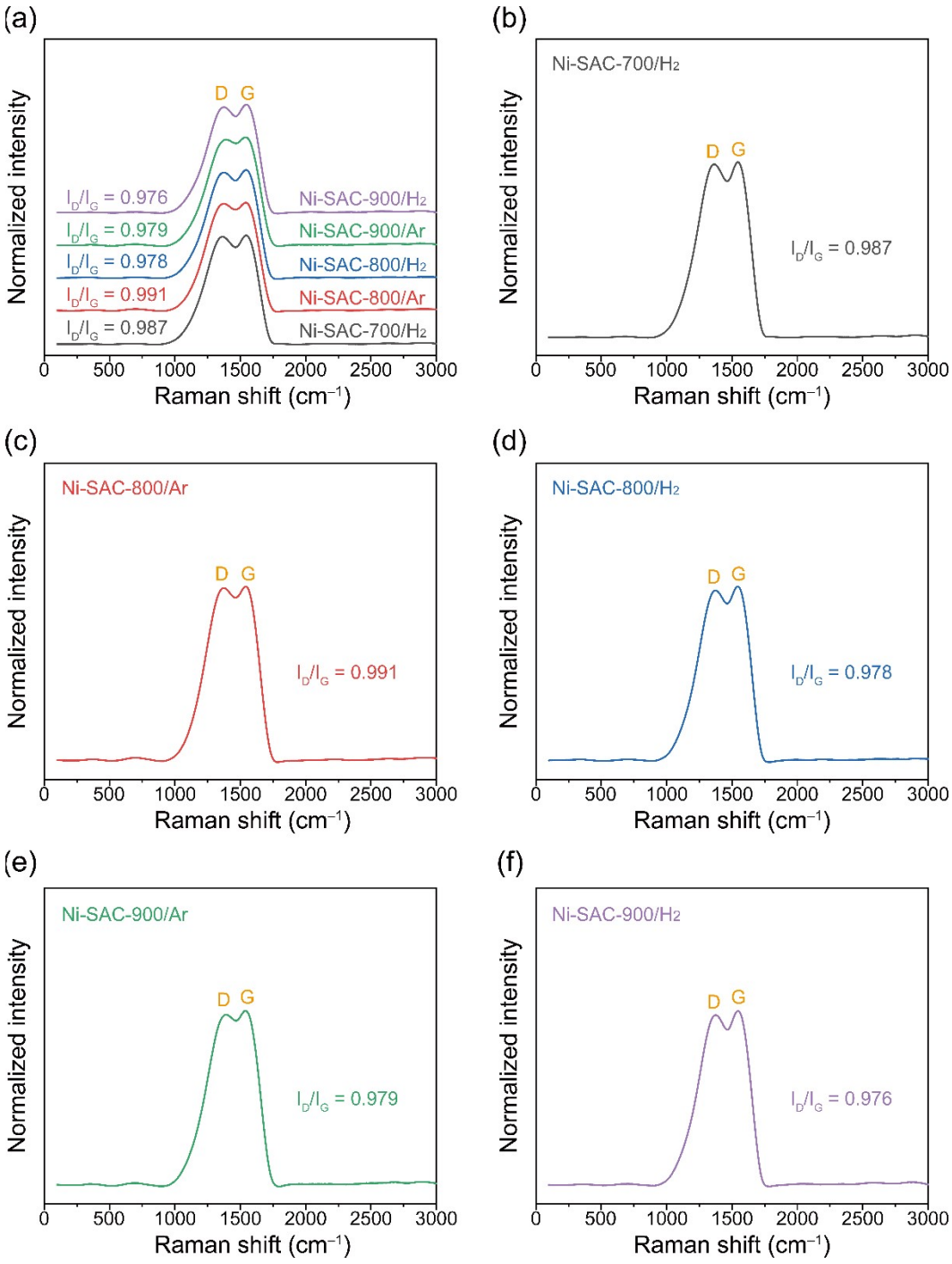

Fig. S5. Raman spectra for a series of Ni-SACs.

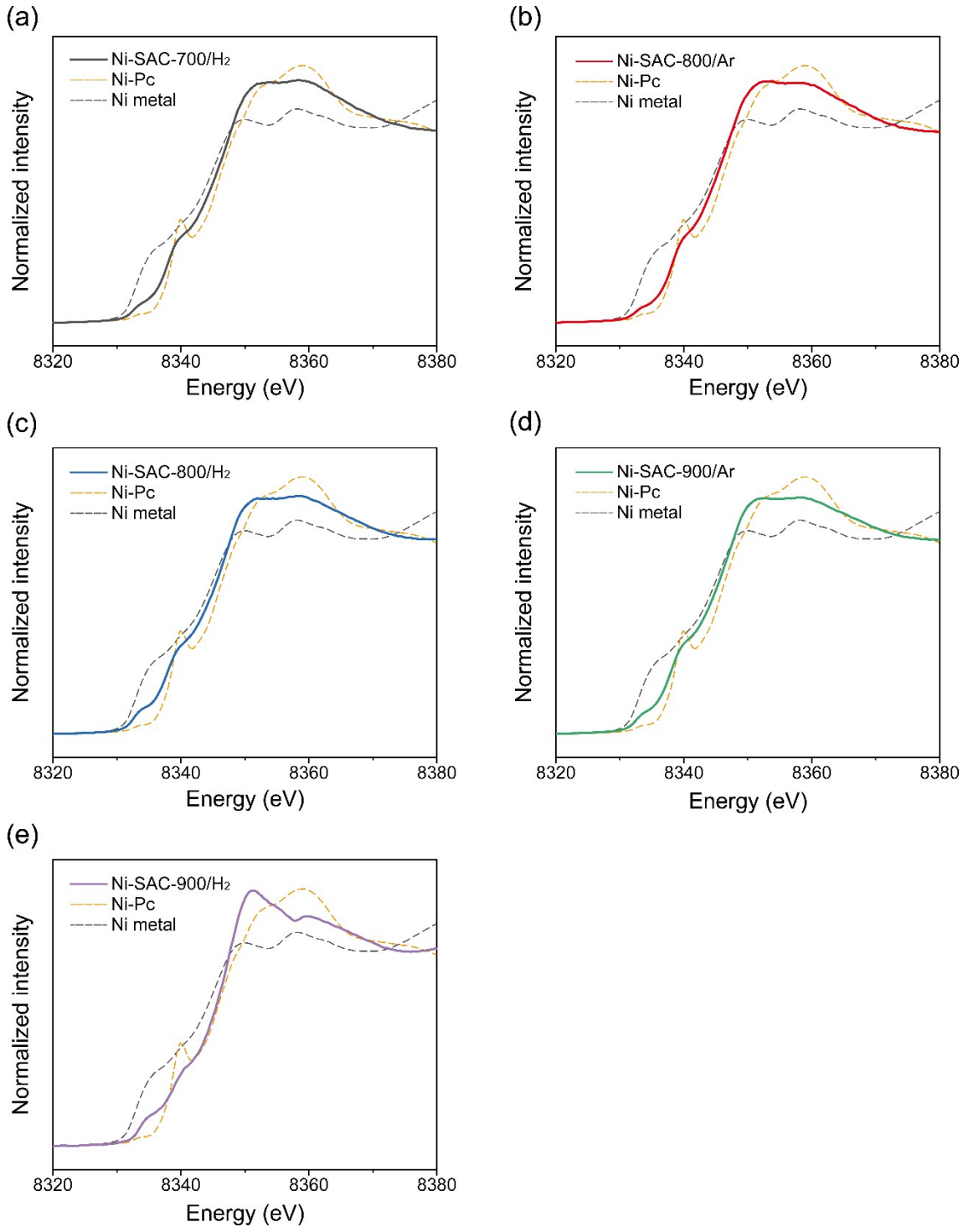

Fig. S6. XANES characterization for a series of Ni-SACs.

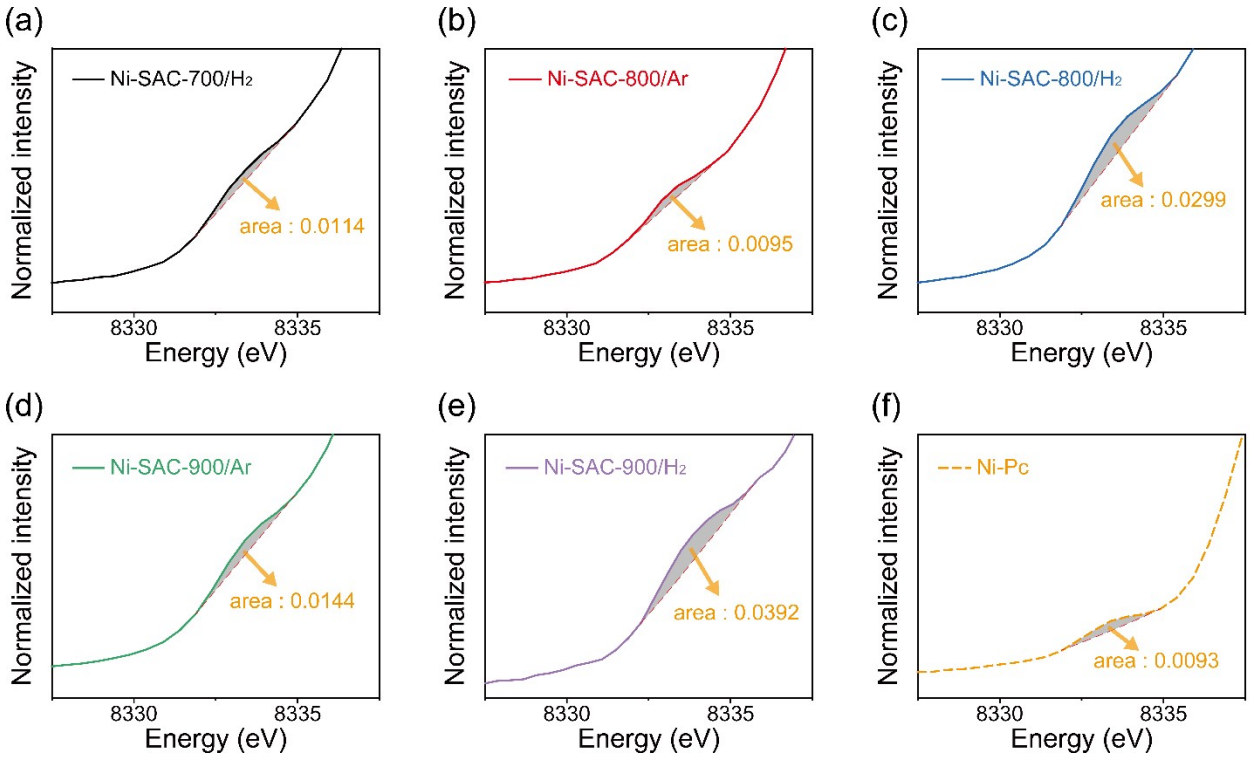

Fig. S7. The integrated area of the **peak A** for the series of Ni-SACs.

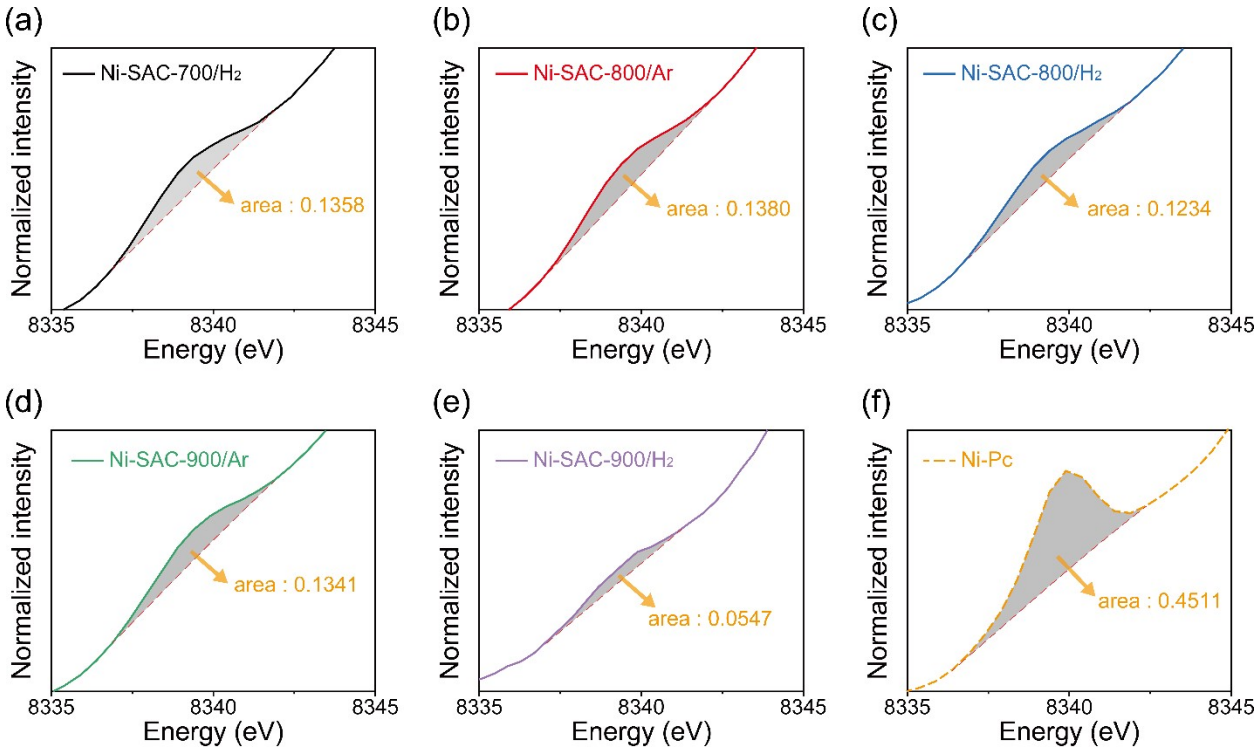

Fig. S8. The integrated area of the **peak B** for the series of Ni-SACs.

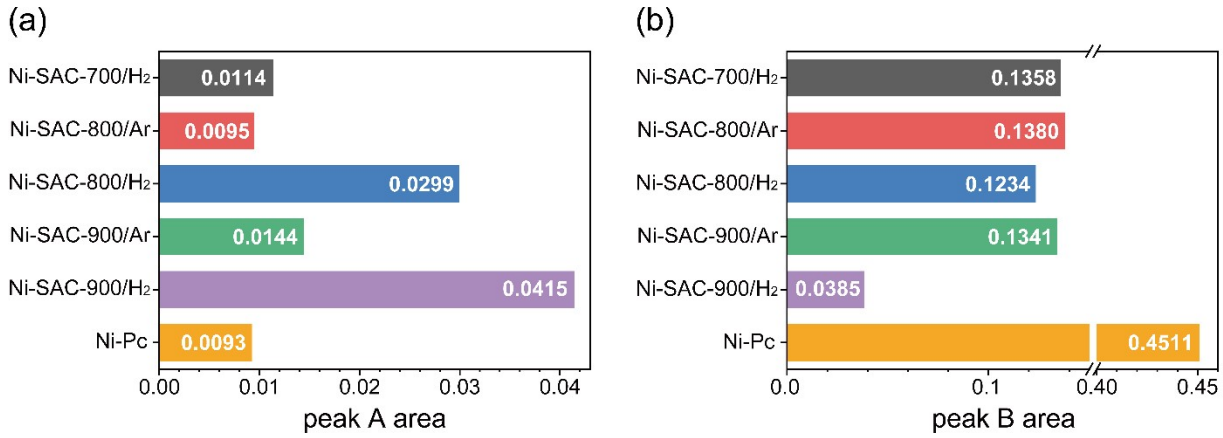

Fig. S9. Integrated area values of a series of catalysts for (a) **peak A** and (b) **peak B** in **Fig. S6-S8**.

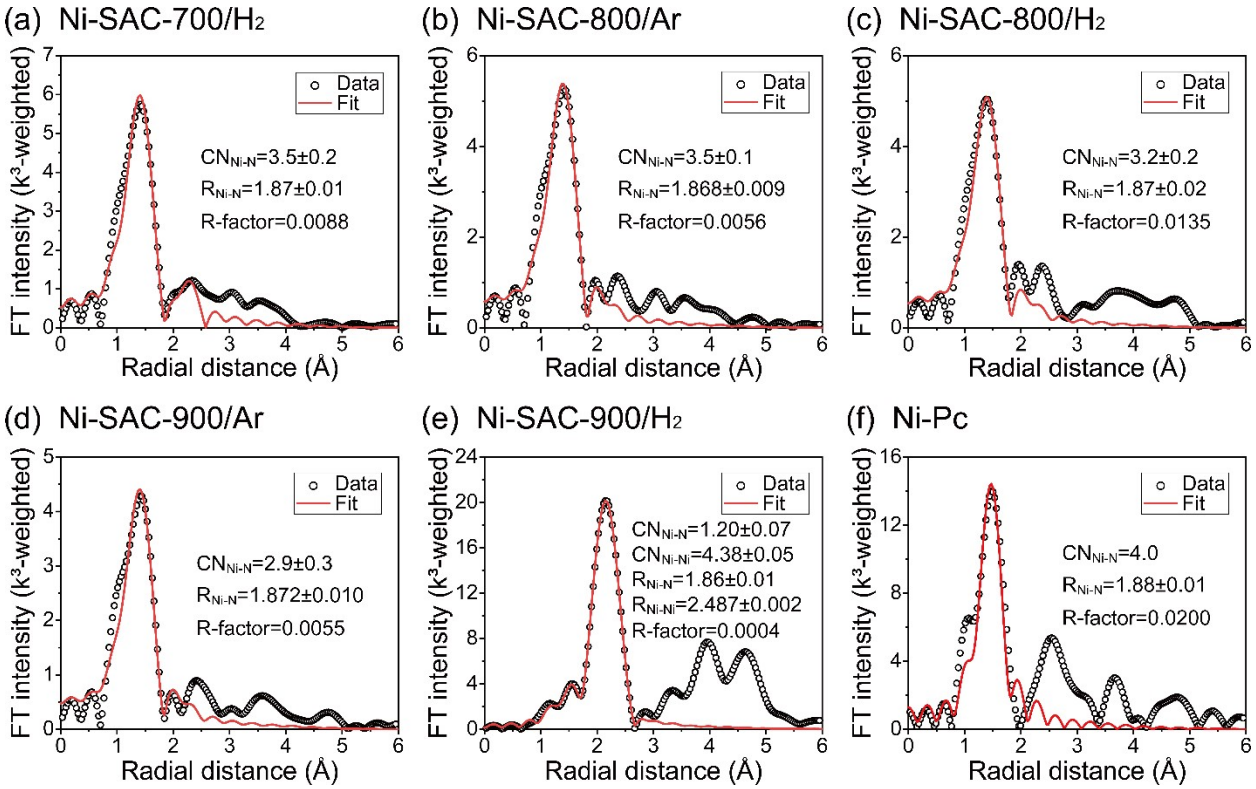

Fig. S10. EXAFS fitting profiles for (a) Ni-SAC-700/H_2, (b) Ni-SAC-800/Ar, (c) Ni-SAC-800/H_2, (d) Ni-SAC-900/Ar, (e) Ni-SAC-900/H_2, and (f) Ni-Pc.

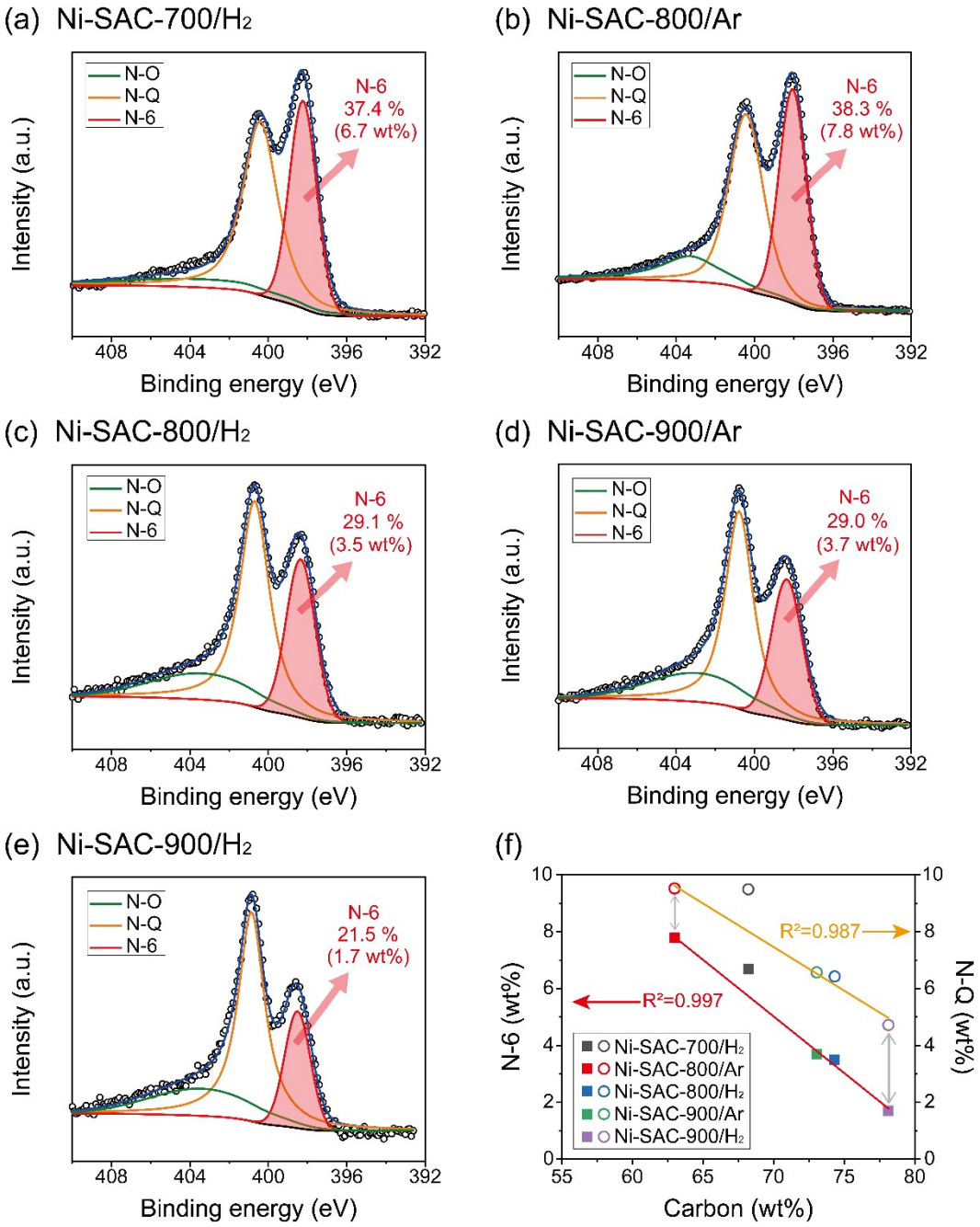

Fig. S11. (a-e) High resolution N 1s spectra of the samples. (f) The correlation of the carbon content with N-6 and N-Q contents.

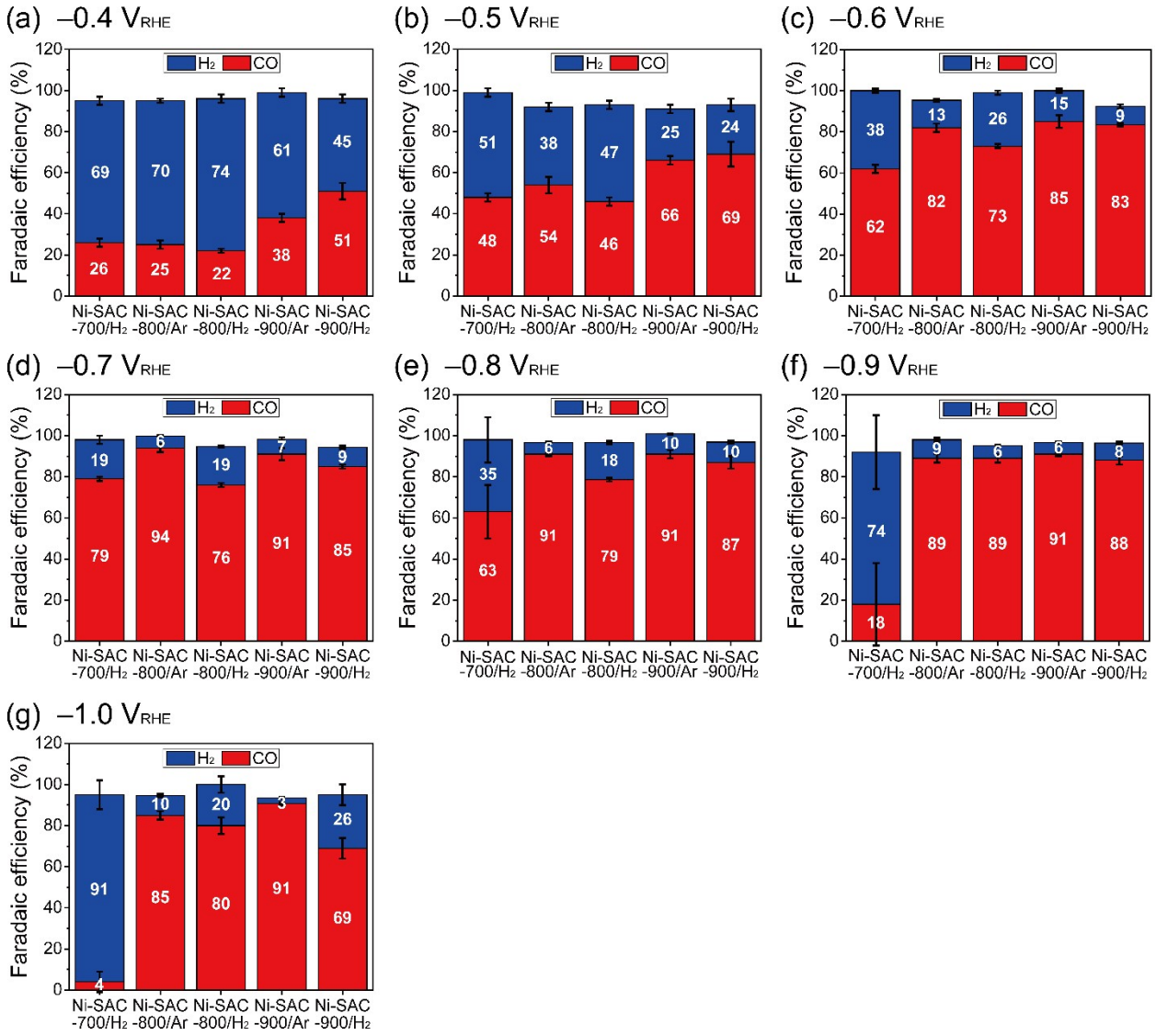

Fig. S12. Faradaic efficiencies for CO and H_2 of the series of Ni-SACs at different potentials.

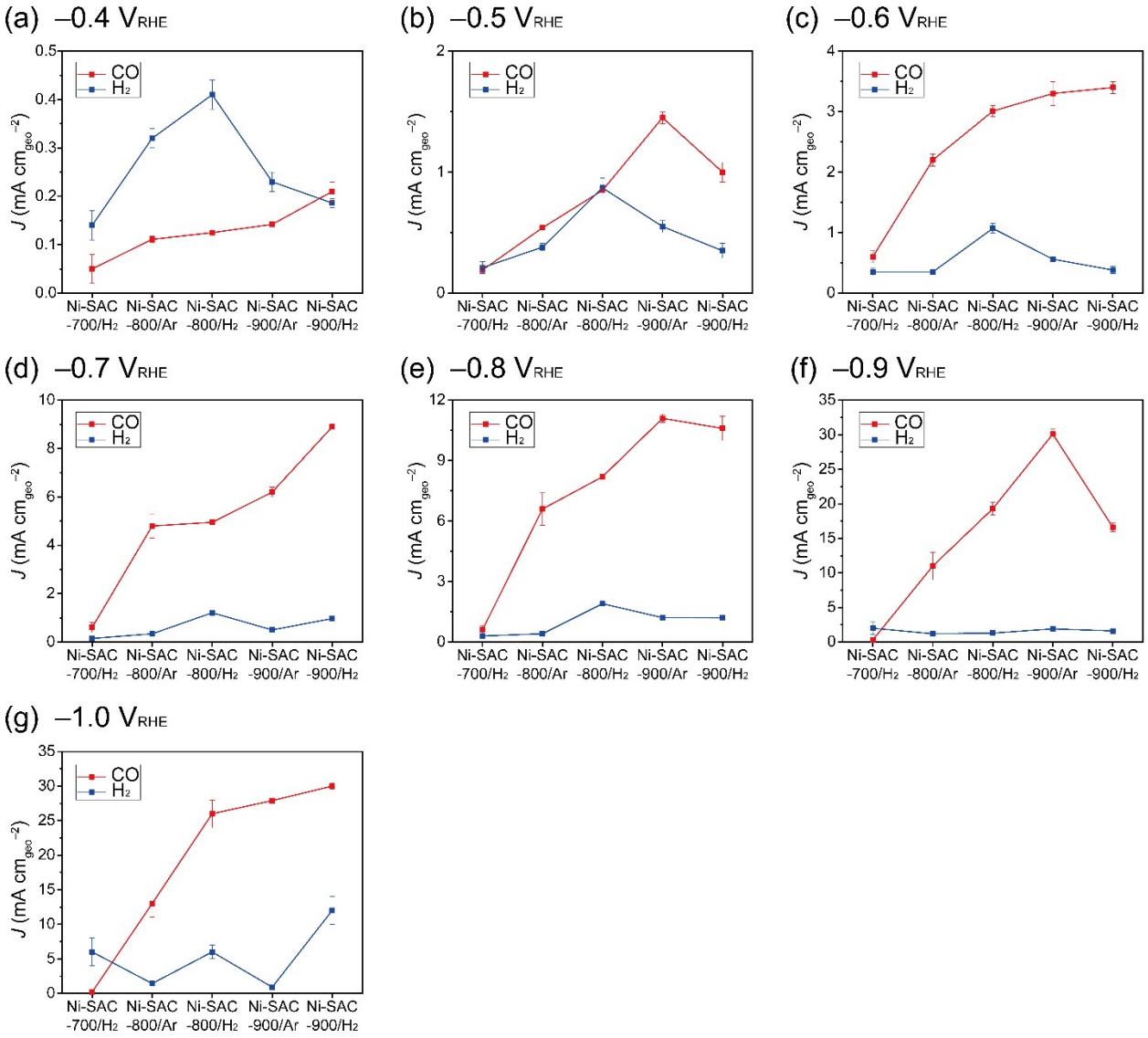

Fig. S13. Partial current densities (mA cm_{geo}^{-2}) for CO and H_2 of the series of Ni-SACs at different potentials.

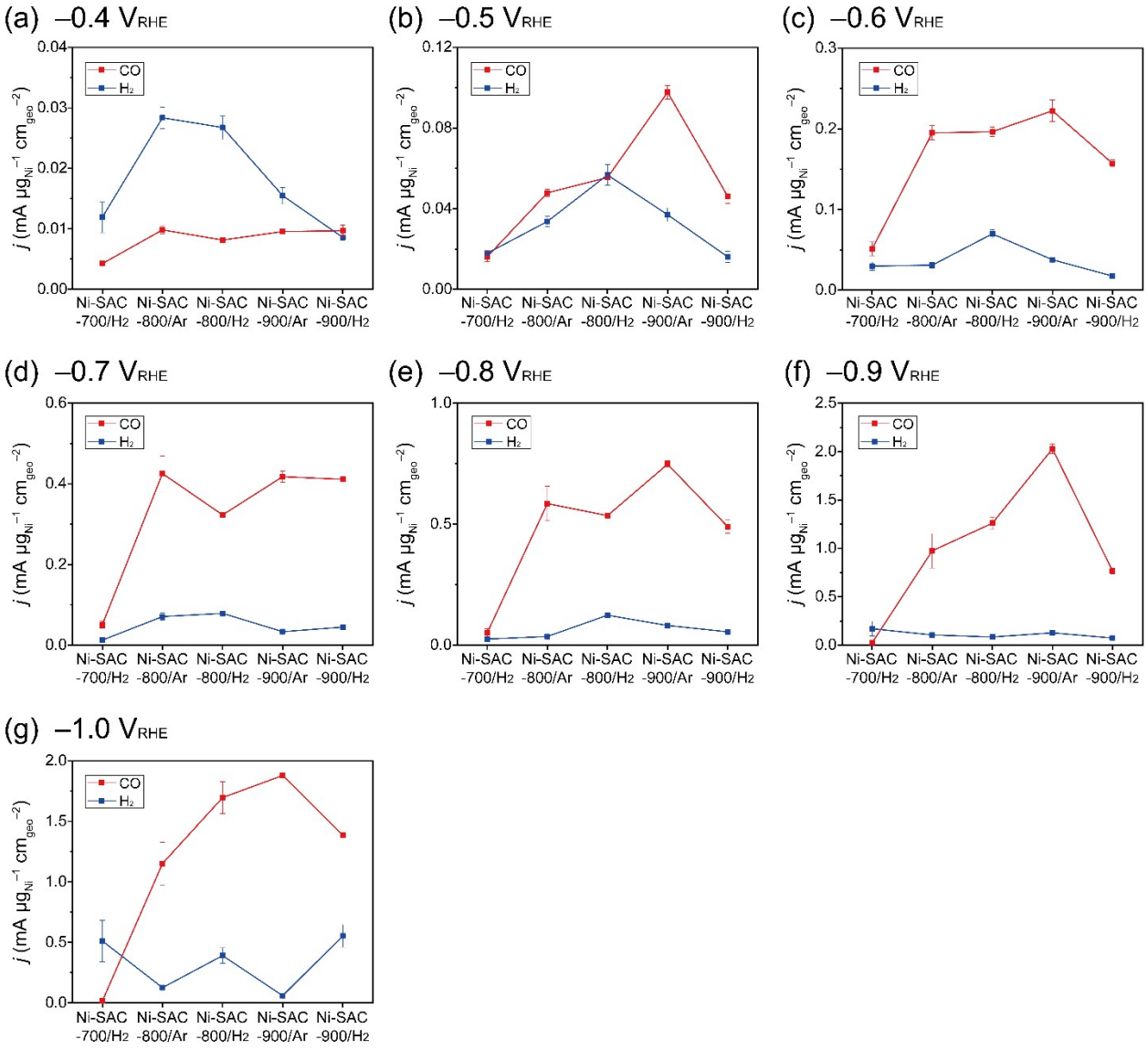

Fig. S14. Normalized partial current densities (mA μg_{Ni}^{-1} cm_{geo}^{-2}) for CO and H_2 of the series of Ni-SACs at different potentials.

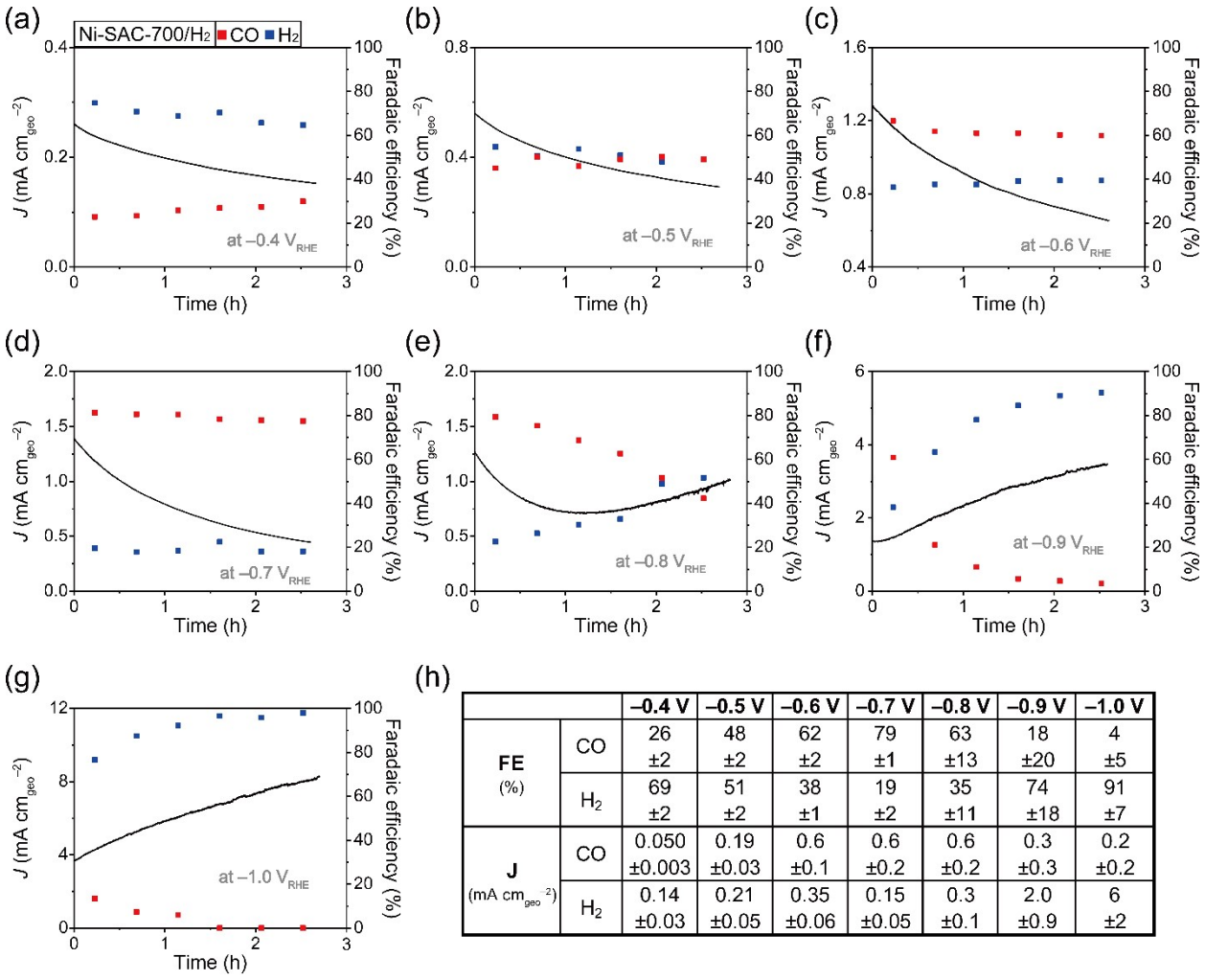

(h)

		–0.4 V	–0.5 V	–0.6 V	–0.7 V	–0.8 V	–0.9 V	–1.0 V
FE (%)	CO	26 ±2	48 ±2	62 ±2	79 ±1	63 ±13	18 ±20	4 ±5
	H_2	69 ±2	51 ±2	38 ±1	19 ±2	35 ±11	74 ±18	91 ±7
J ($mA\ cm_{geo}^{-2}$)	CO	0.050 ±0.003	0.19 ±0.03	0.6 ±0.1	0.6 ±0.2	0.6 ±0.2	0.3 ±0.3	0.2 ±0.2
	H_2	0.14 ±0.03	0.21 ±0.05	0.35 ±0.06	0.15 ±0.05	0.3 ±0.1	2.0 ±0.9	6 ±2

Fig. S15. Electrochemical performance of Ni-SAC-700/H_2. (a-g) CA curves at different potentials alongside the individual data points of FE_{CO} and FE_{H2}. (h) The calculated FE and J values at different potentials.

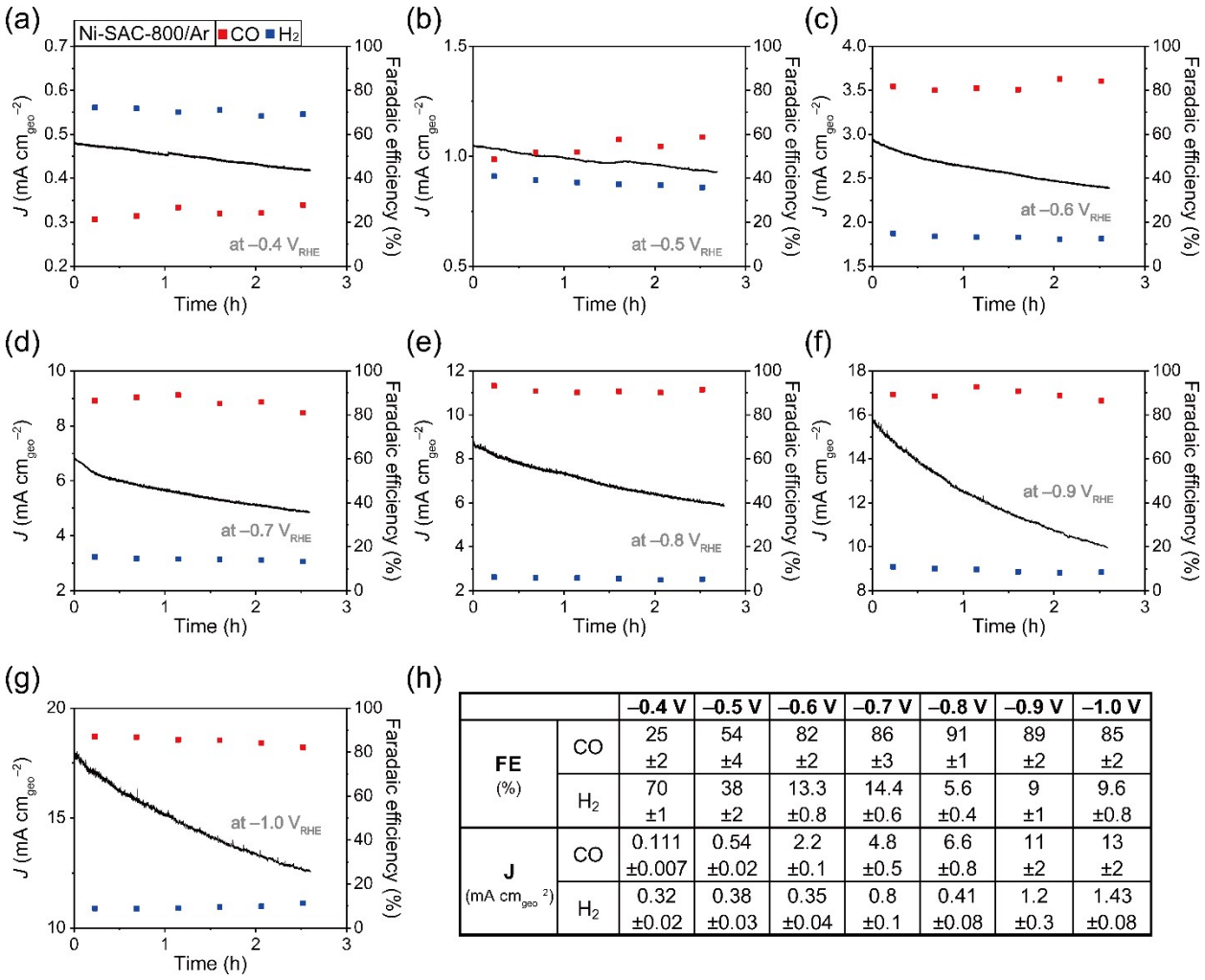

		–0.4 V	–0.5 V	–0.6 V	–0.7 V	–0.8 V	–0.9 V	–1.0 V
FE (%)	CO	25 ±2	54 ±4	82 ±2	86 ±3	91 ±1	89 ±2	85 ±2
	H_2	70 ±1	38 ±2	13.3 ±0.8	14.4 ±0.6	5.6 ±0.4	9 ±1	9.6 ±0.8
J (mA cm_{geo}^{-2})	CO	0.111 ±0.007	0.54 ±0.02	2.2 ±0.1	4.8 ±0.5	6.6 ±0.8	11 ±2	13 ±2
	H_2	0.32 ±0.02	0.38 ±0.03	0.35 ±0.04	0.8 ±0.1	0.41 ±0.08	1.2 ±0.3	1.43 ±0.08

Fig. S16. Faradaic efficiency and current density at different potentials of Ni-SAC-800/Ar.

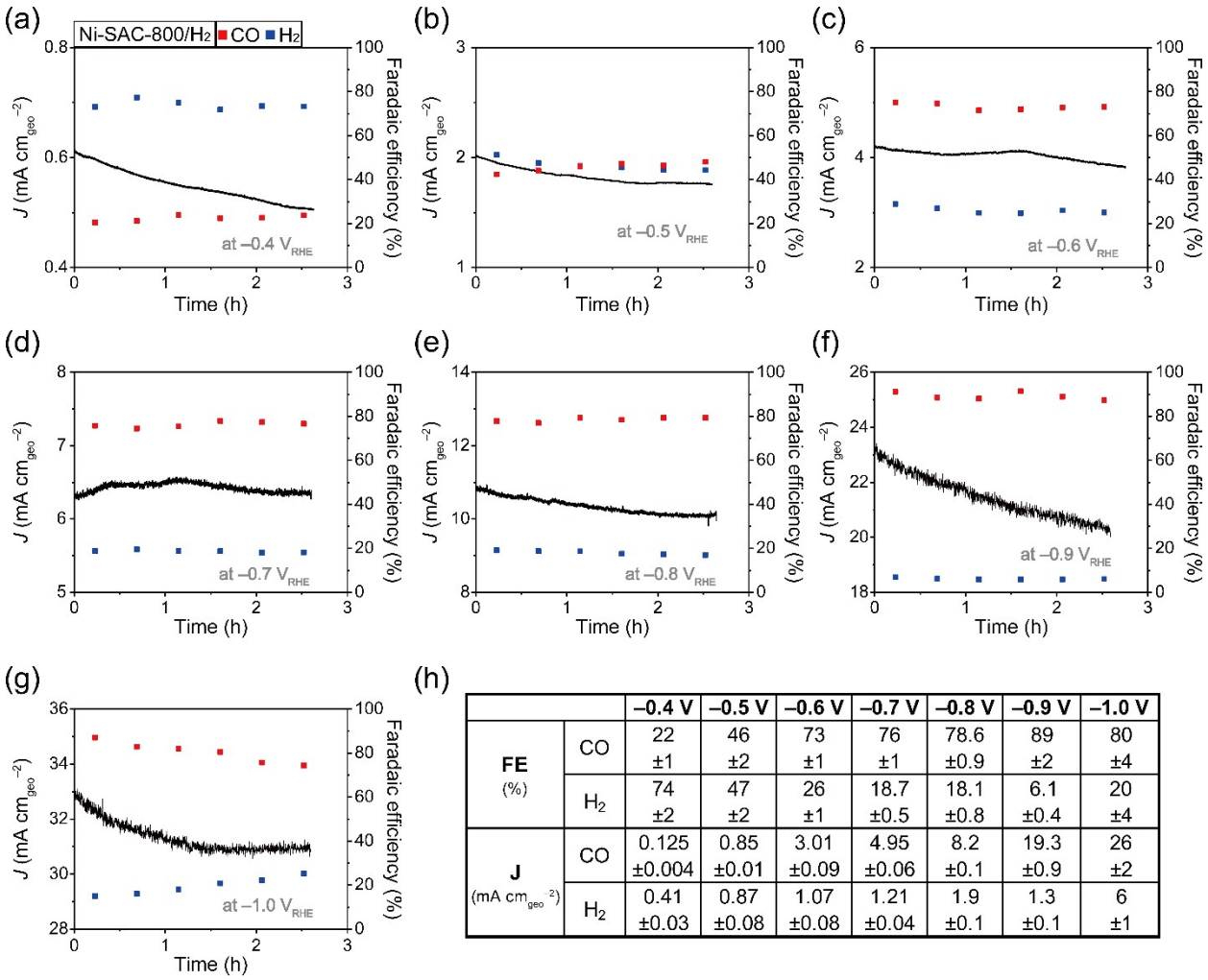

(h)

		–0.4 V	–0.5 V	–0.6 V	–0.7 V	–0.8 V	–0.9 V	–1.0 V
FE (%)	CO	22 ±1	46 ±2	73 ±1	76 ±1	78.6 ±0.9	89 ±2	80 ±4
	H_2	74 ±2	47 ±2	26 ±1	18.7 ±0.5	18.1 ±0.8	6.1 ±0.4	20 ±4
J (mA cm_{geo}^{-2})	CO	0.125 ±0.004	0.85 ±0.01	3.01 ±0.09	4.95 ±0.06	8.2 ±0.1	19.3 ±0.9	26 ±2
	H_2	0.41 ±0.03	0.87 ±0.08	1.07 ±0.08	1.21 ±0.04	1.9 ±0.1	1.3 ±0.1	6 ±1

Fig. S17. Faradaic efficiency and current density at different potentials of Ni-SAC-800/H_2.

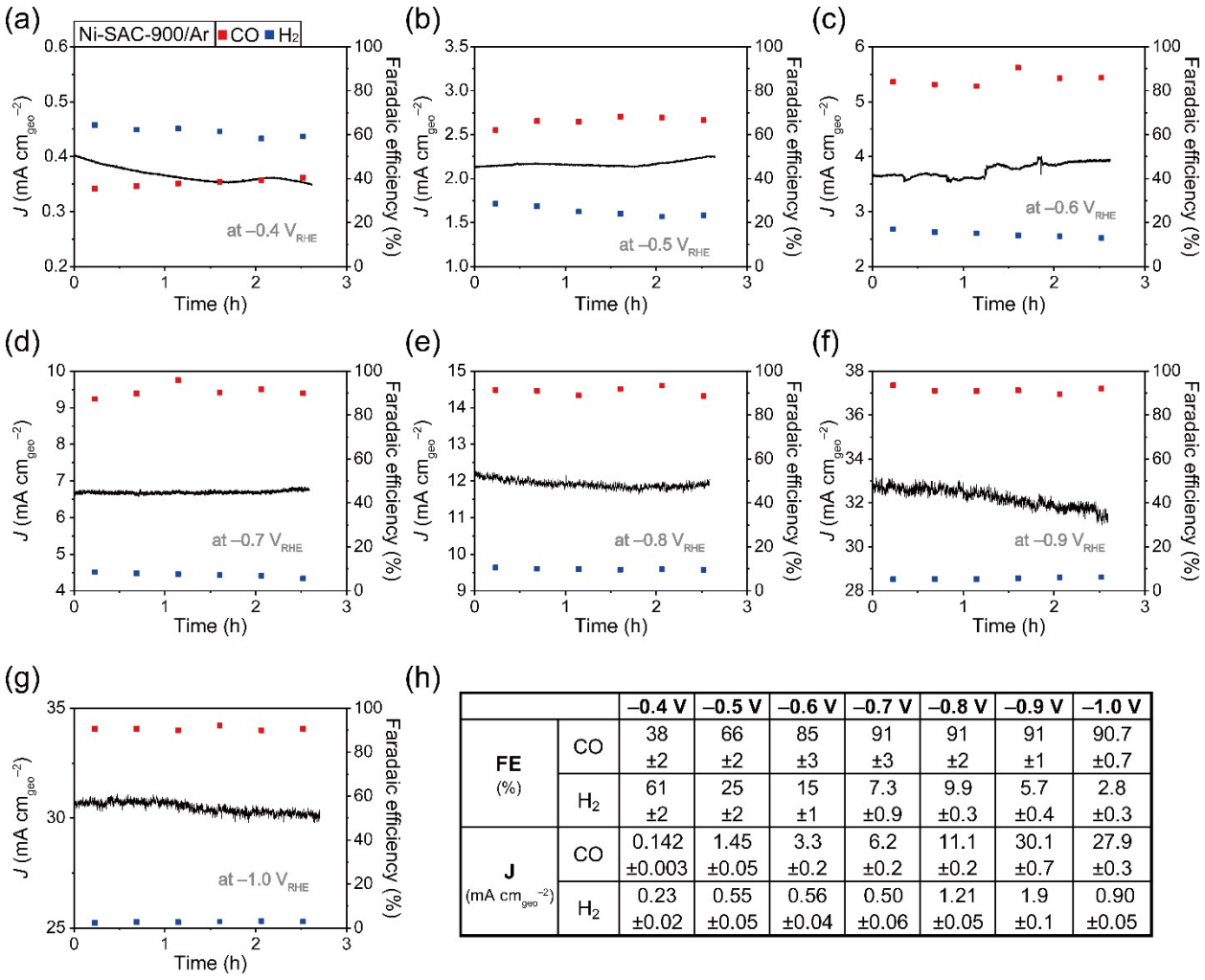

(h)

		–0.4 V	–0.5 V	–0.6 V	–0.7 V	–0.8 V	–0.9 V	–1.0 V
FE (%)	CO	38 ±2	66 ±2	85 ±3	91 ±3	91 ±2	91 ±1	90.7 ±0.7
	H_2	61 ±2	25 ±2	15 ±1	7.3 ±0.9	9.9 ±0.3	5.7 ±0.4	2.8 ±0.3
J (mA cm_{geo}^{-2})	CO	0.142 ±0.003	1.45 ±0.05	3.3 ±0.2	6.2 ±0.2	11.1 ±0.2	30.1 ±0.7	27.9 ±0.3
	H_2	0.23 ±0.02	0.55 ±0.05	0.56 ±0.04	0.50 ±0.06	1.21 ±0.05	1.9 ±0.1	0.90 ±0.05

Fig. S18. Faradaic efficiency and current density at different potentials of Ni-SAC-900/Ar.

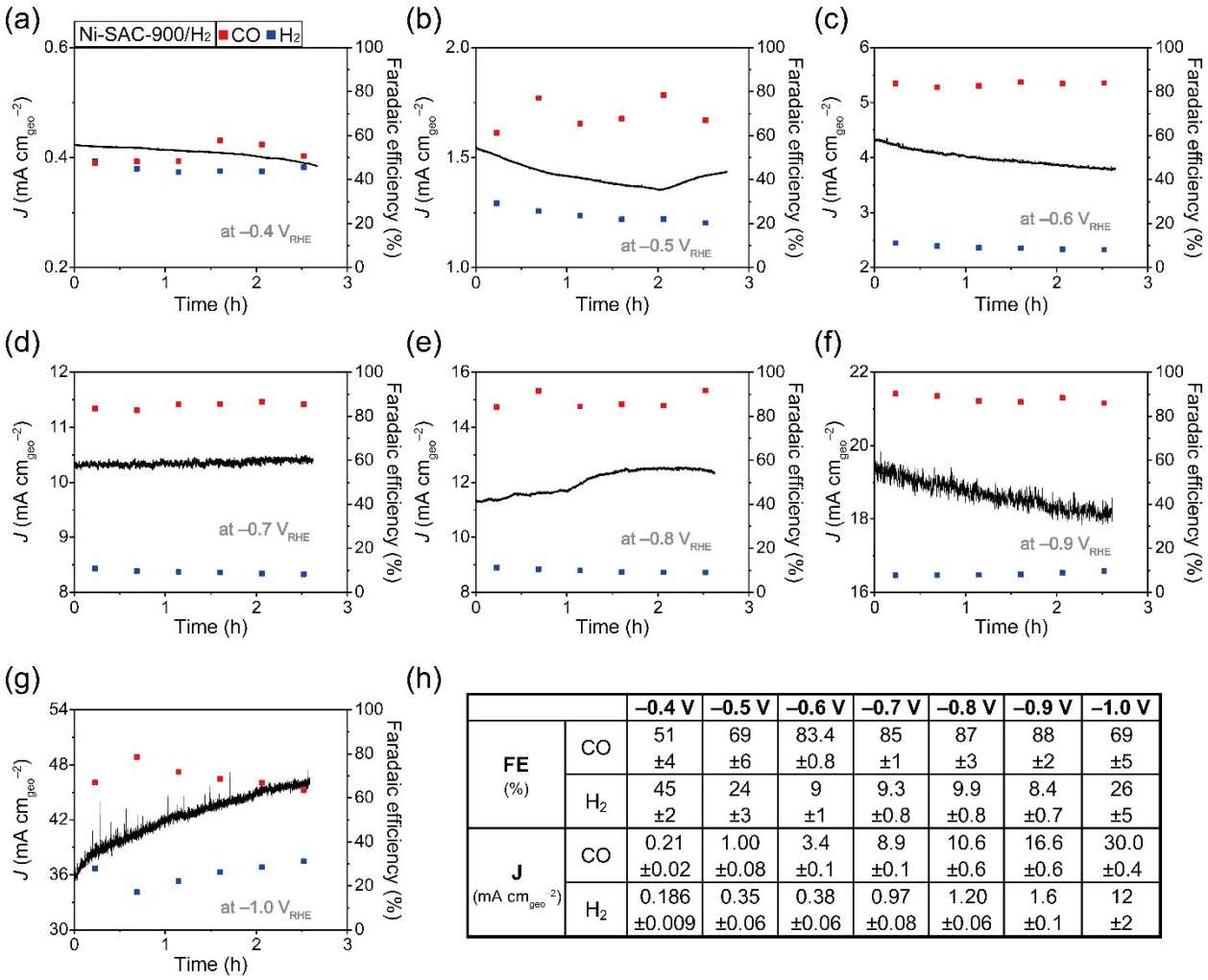

(h)

		–0.4 V	–0.5 V	–0.6 V	–0.7 V	–0.8 V	–0.9 V	–1.0 V
FE (%)	CO	51 ±4	69 ±6	83.4 ±0.8	85 ±1	87 ±3	88 ±2	69 ±5
	H_2	45 ±2	24 ±3	9 ±1	9.3 ±0.8	9.9 ±0.8	8.4 ±0.7	26 ±5
J ($mA\ cm_{geo}^{-2}$)	CO	0.21 ±0.02	1.00 ±0.08	3.4 ±0.1	8.9 ±0.1	10.6 ±0.6	16.6 ±0.6	30.0 ±0.4
	H_2	0.186 ±0.009	0.35 ±0.06	0.38 ±0.06	0.97 ±0.08	1.20 ±0.06	1.6 ±0.1	12 ±2

Fig. S19. Faradaic efficiency and current density at different potentials of Ni-SAC-900/H_2.

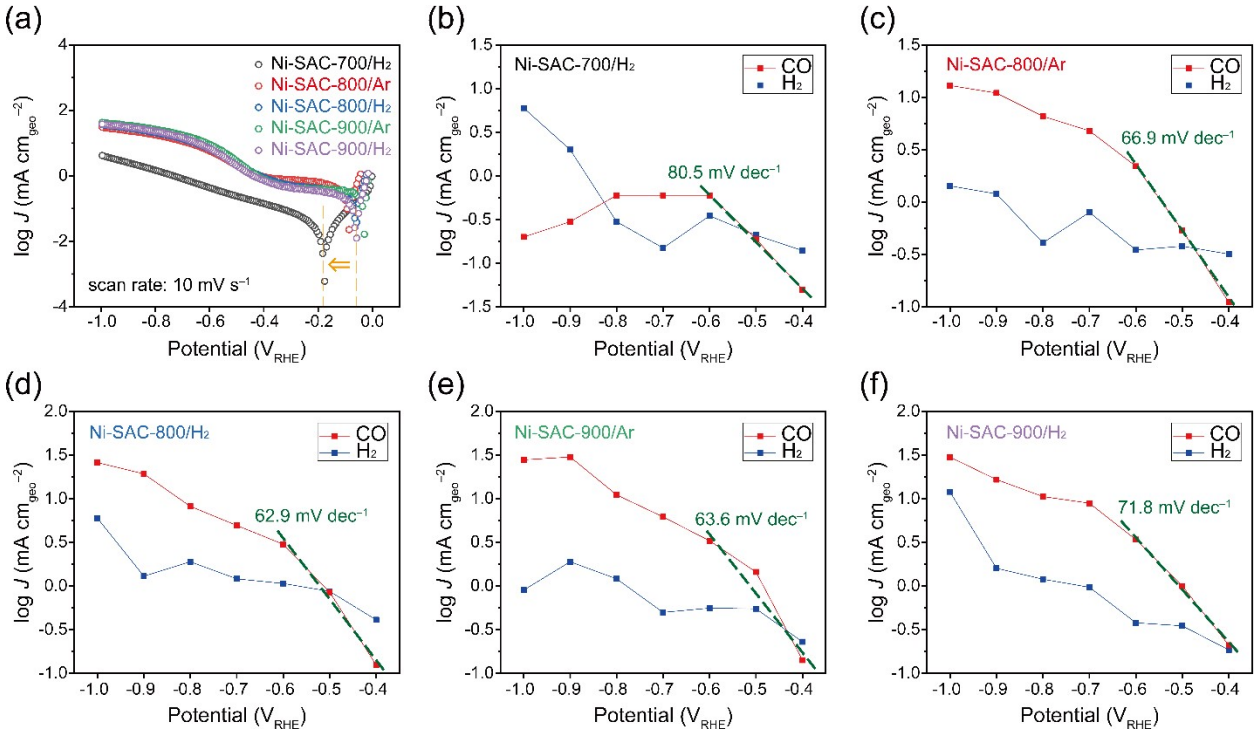

Fig. S20. (a) Tafel plots derived from linear sweep voltammetry (LSV) curves for Ni-SACs. (b) Tafel plots based on J_{CO} and J_{H2} values for Ni-SACs.

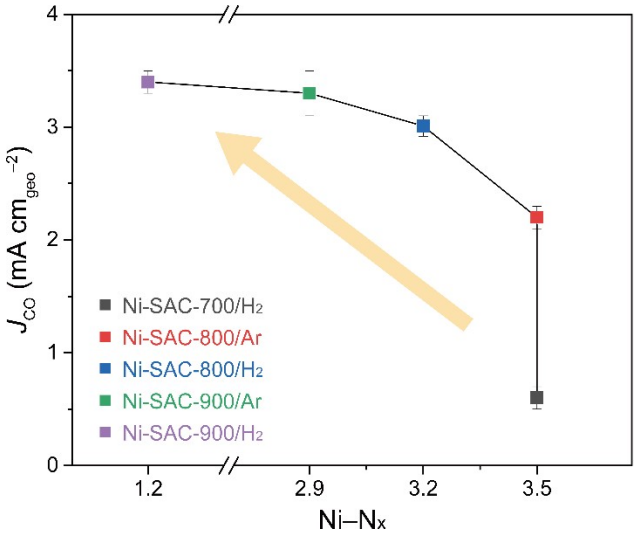

Fig. S21. Correlation between J_{CO} (mA cm_{geo}^{-2} at –0.6 V_{RHE}) and N coordination (x) for a series of Ni-SACs.

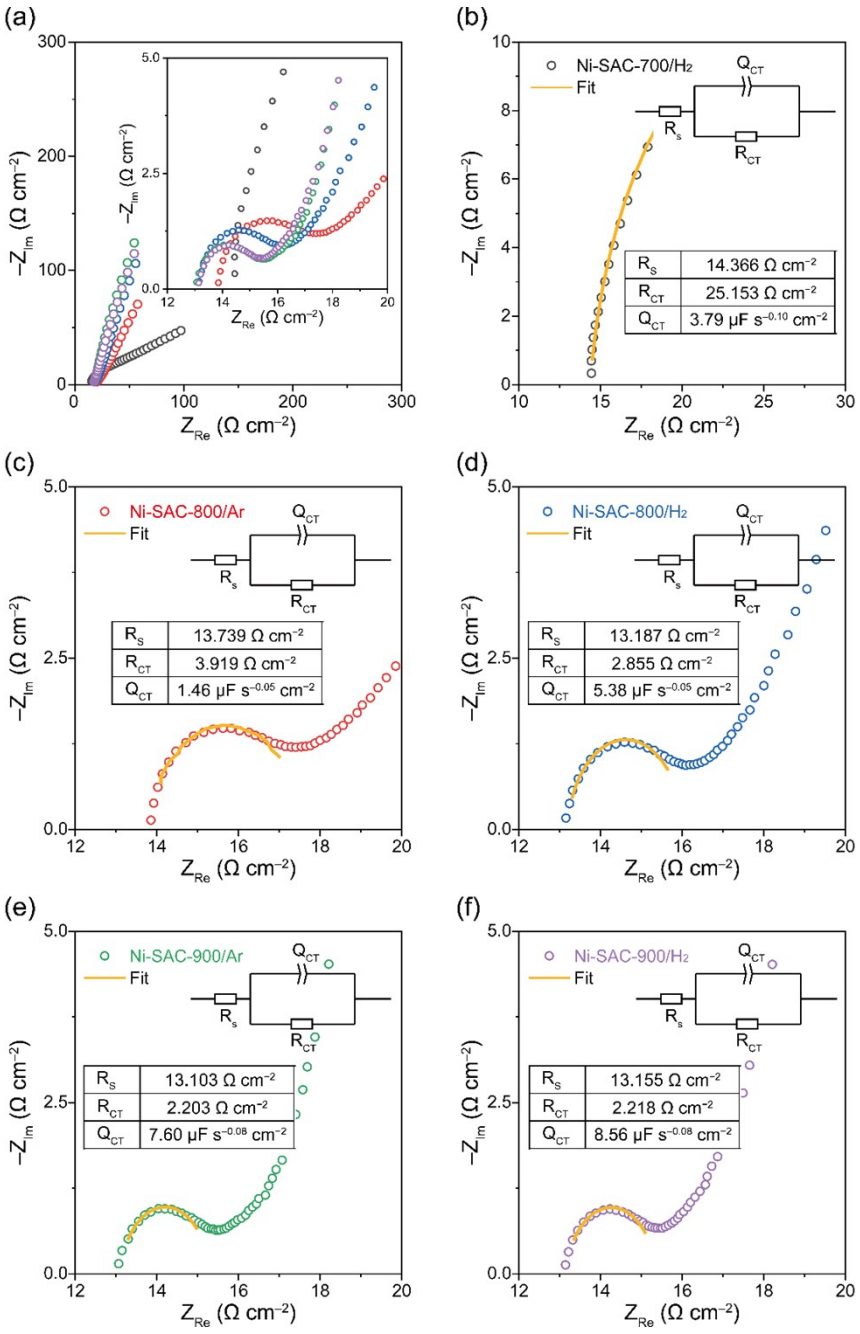

Fig. S22. (a) EIS analyses for series of Ni-SACs. Inset is a magnified EIS profile to visualize the semicircle region. EIS fitting results for (b) Ni-SAC-700/H_2, (c) Ni-SAC-800/Ar, (d) Ni-SAC-800/H_2, (e) Ni-SAC-900/Ar, and (f) Ni-SAC-900/H_2. Inset is the electrochemical equivalent circuit model for the fitting.

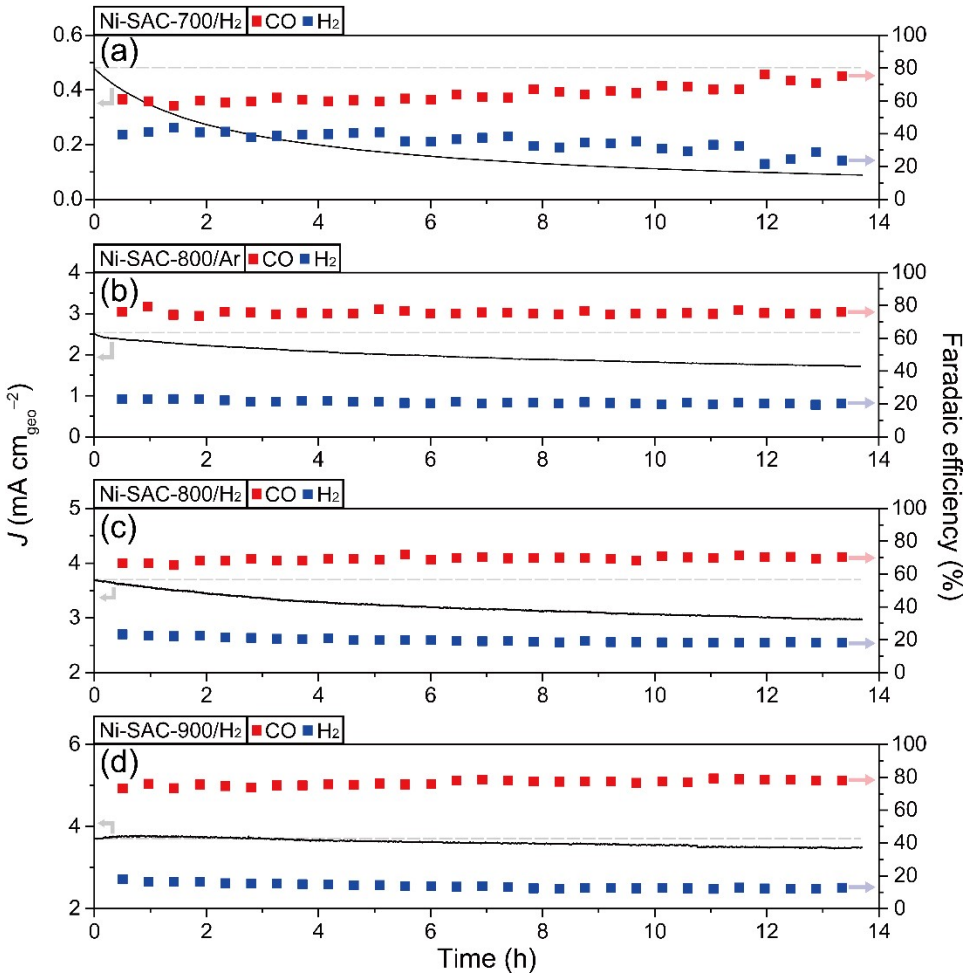

Fig. S23. Stability tests of (a) Ni-SAC-700/H_2, (b) Ni-SAC-800/Ar, (c) Ni-SAC-800/H_2, and (d) Ni-SAC-900/H_2 performed at –0.6 V_{RHE}.

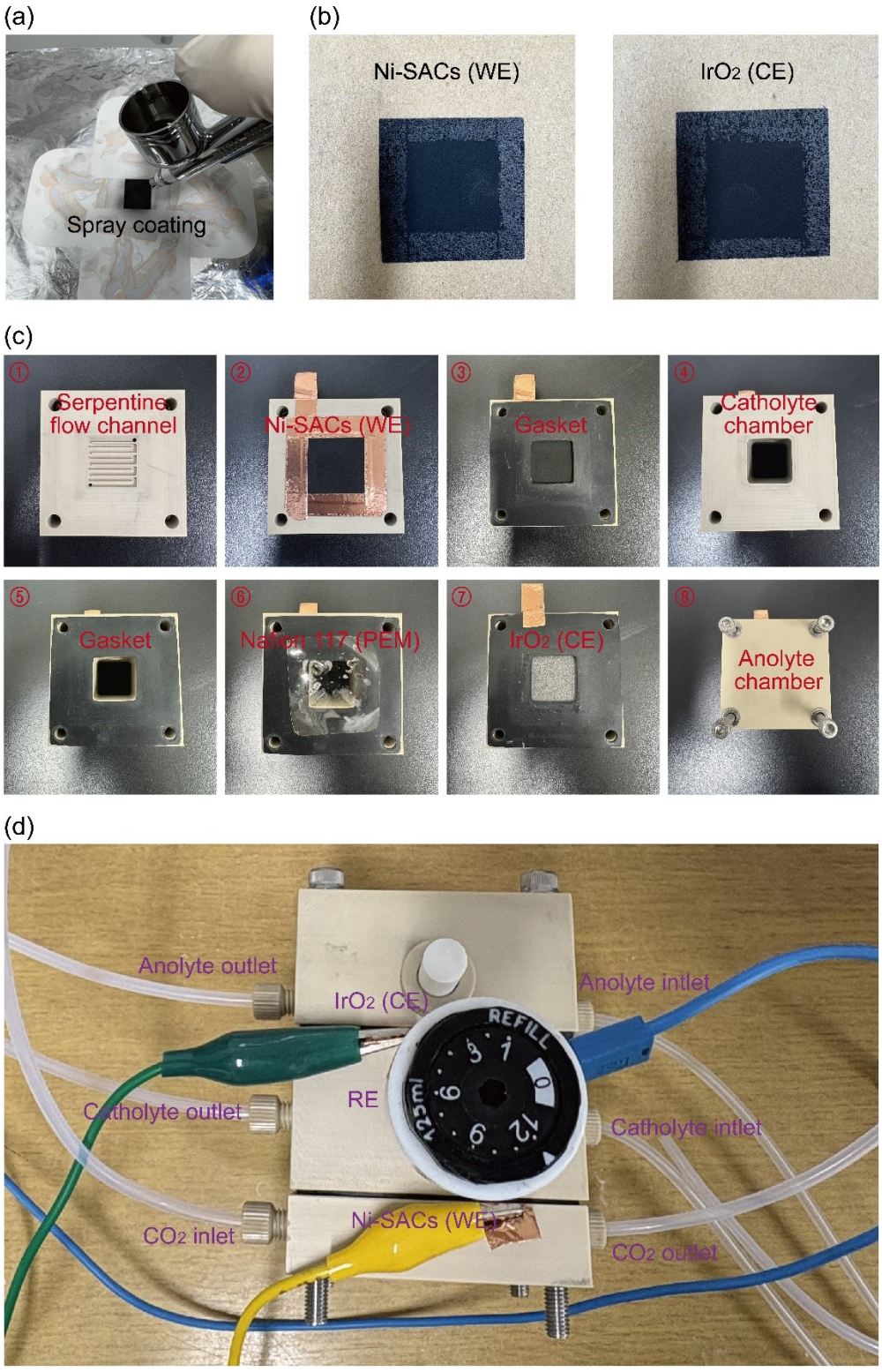

Fig. S24. (a) Photographs of spray coating for electrodes and (b) vacuum-dried WE and CE. (c-d) Photographs of step-by-step cell assembly for our flow cell reactor.

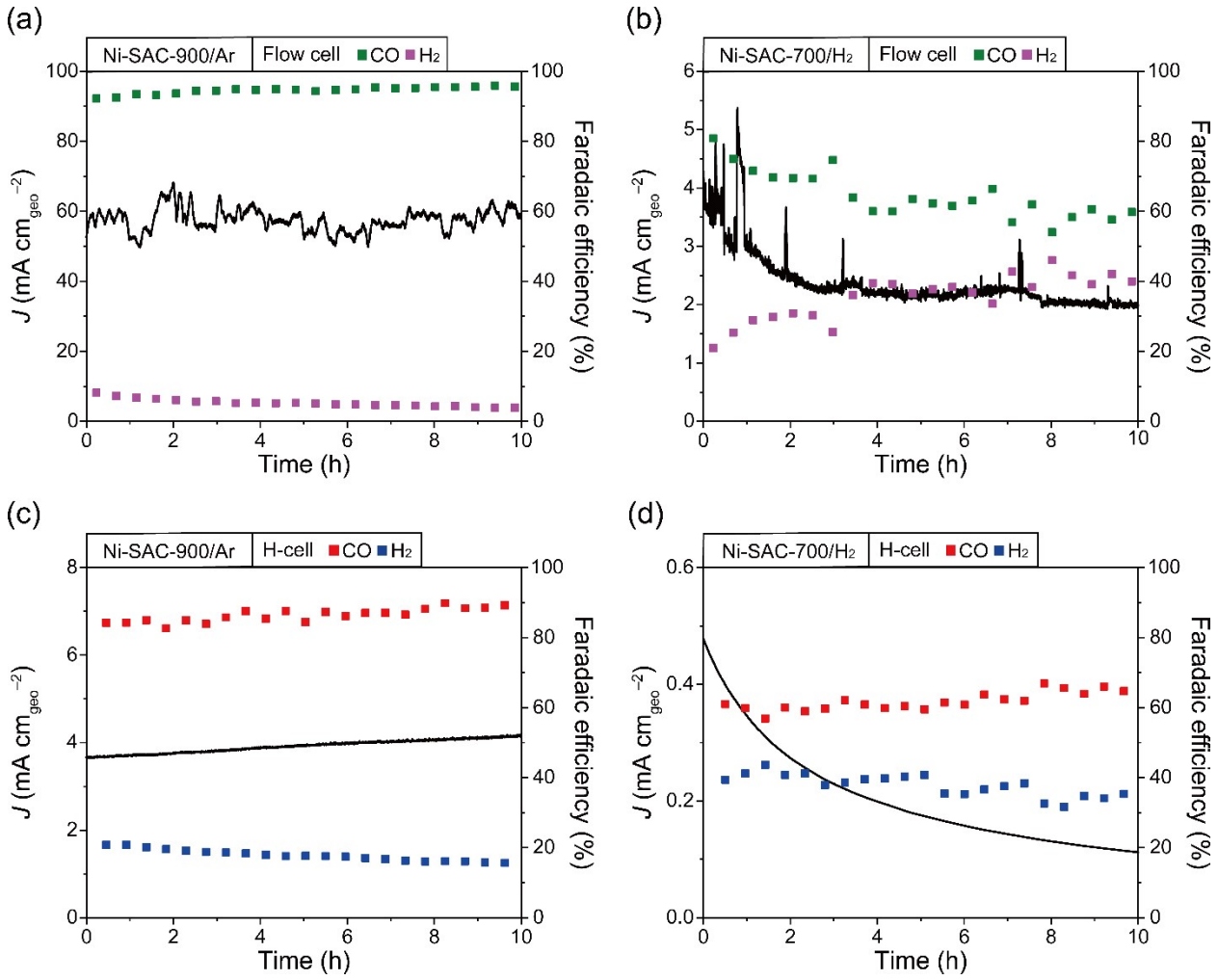

Fig. S25. CO_2RR performance comparison of Ni-SAC-900/Ar and Ni-SAC-700/H_2. (a-b) Satability tests at (a-b) flow cell and (c-d) H-cell setups.

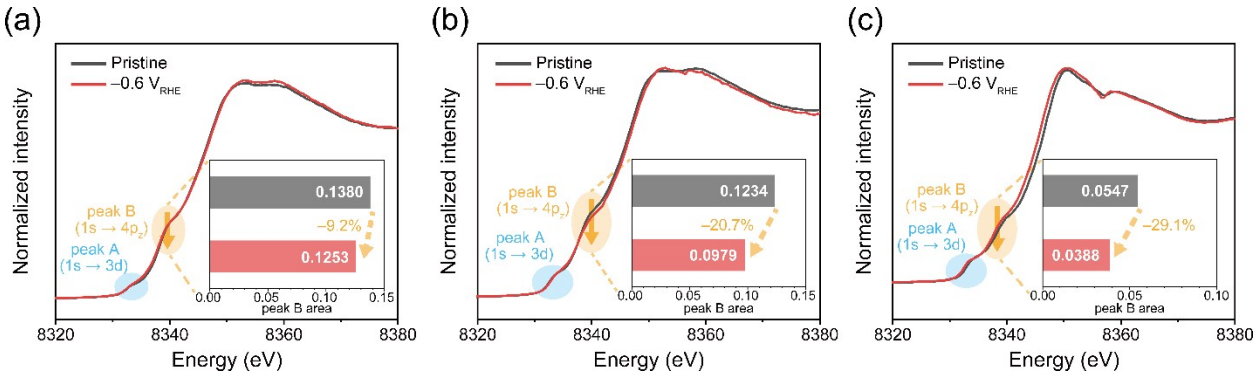

Fig. S26. *In-situ* XANES results of (a) Ni-SAC-800/Ar, (b) Ni-SAC-800/H_2, and (c) Ni-SAC-900/H_2 at Ni K-edge.

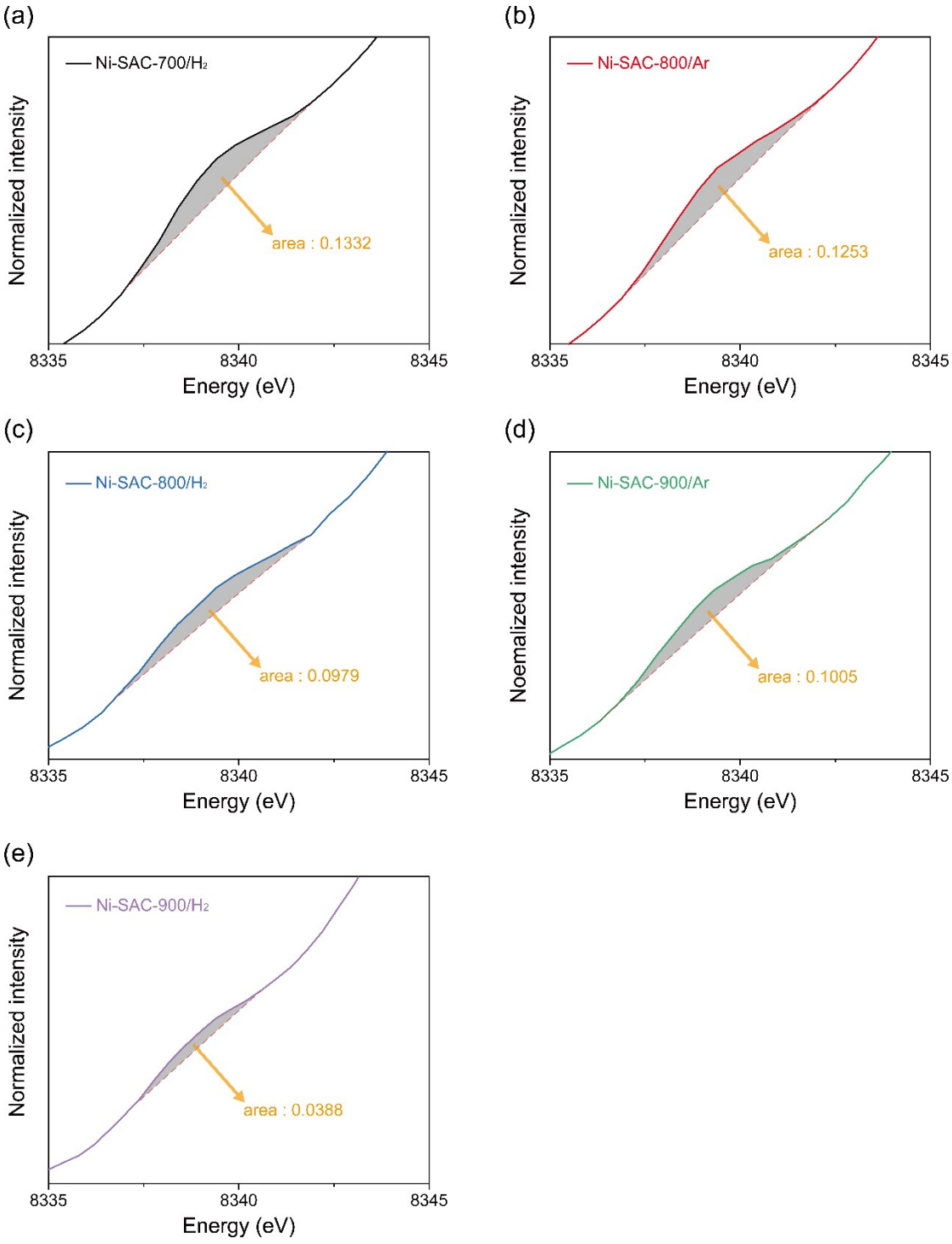

Fig. S27. Integrated area values for **peak B** of (a) Ni-SAC-700/H_2, (b) Ni-SAC-800/Ar, (c) Ni-SAC-800/H_2, (d) Ni-SAC-900/Ar, and (e) Ni-SAC-900/H_2 at –0.6 V_{RHE}.

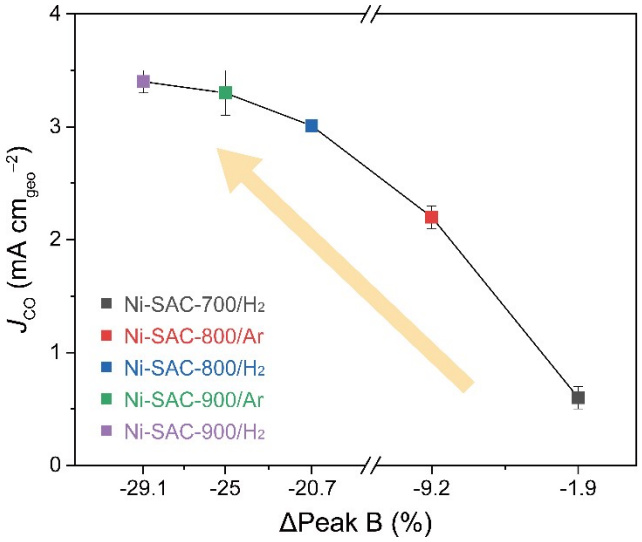

Fig. S28. Correlation between J_{CO} (mA cm_{geo}^{-2} at –0.6 V_{RHE}) and ΔPeak B (%) for a series of Ni-SACs.

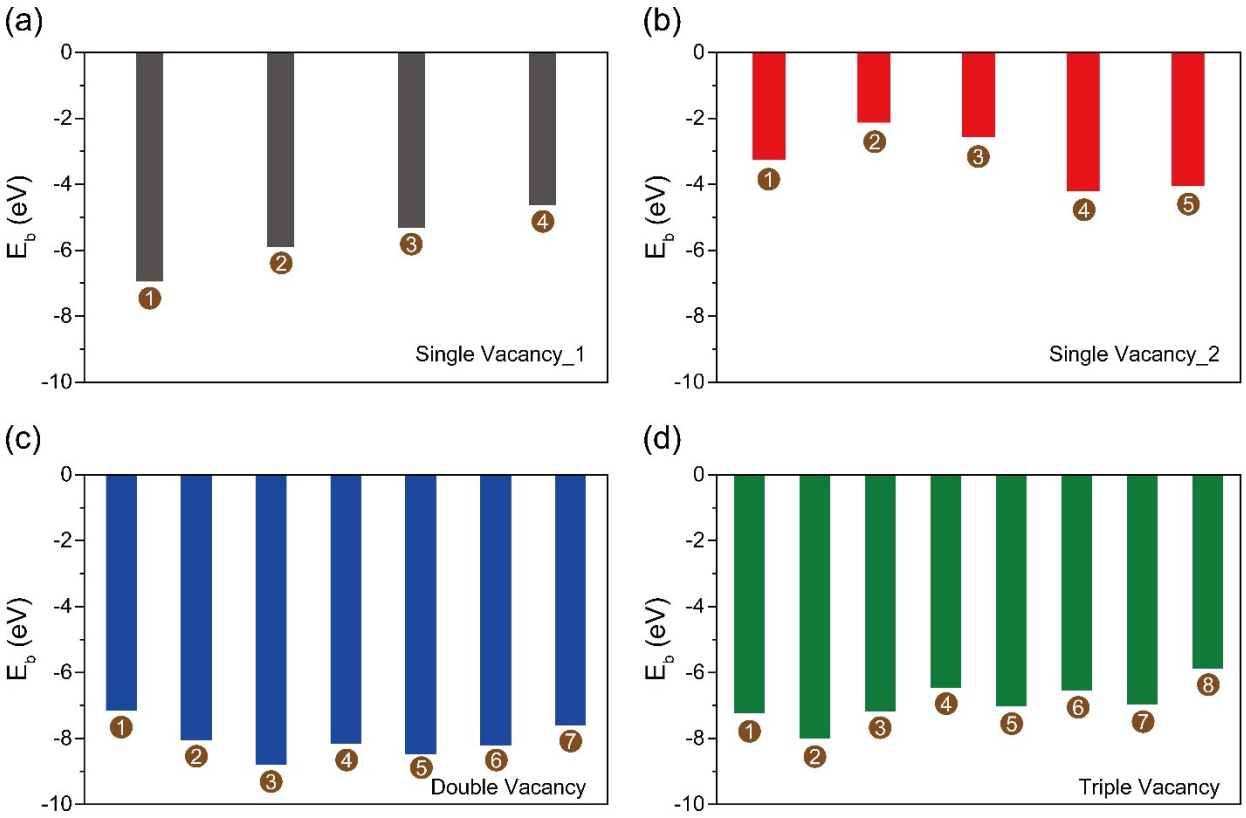

Fig. S29. The binding energy of Ni atom on different Ni-SAC. The black, red, blue, and green bars represent (a) NiNxCy-SV1, (b) NiNxCy-SV2, (c) NiNxCy-DV, and (d) NiNxCy-TV respectively.

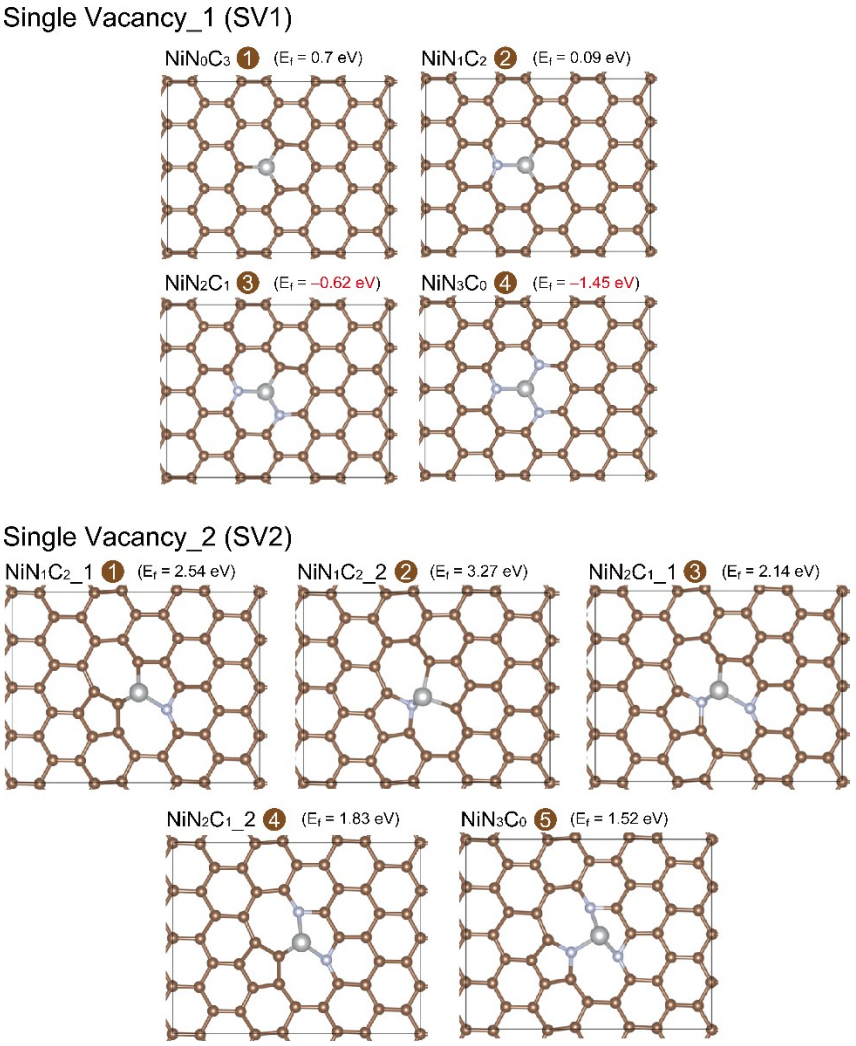

Fig. S30. Optimized structures Ni-SACs. For NiN_xC_y, x and y represent the number of N atoms and C atoms connected with the Ni atom. For SV1 and SV2, the Ni is coordinated to 3 sites on the graphene surface. The Ni-bonded C coordination number is 3-x. NiN_xC_y_i (i=1, 2, and 3) represent a specific N decoration on the graphene surface with the same x and y. Certain Ni-SACs have a single configuration, *i.e.*, one type of nitrogen decoration.

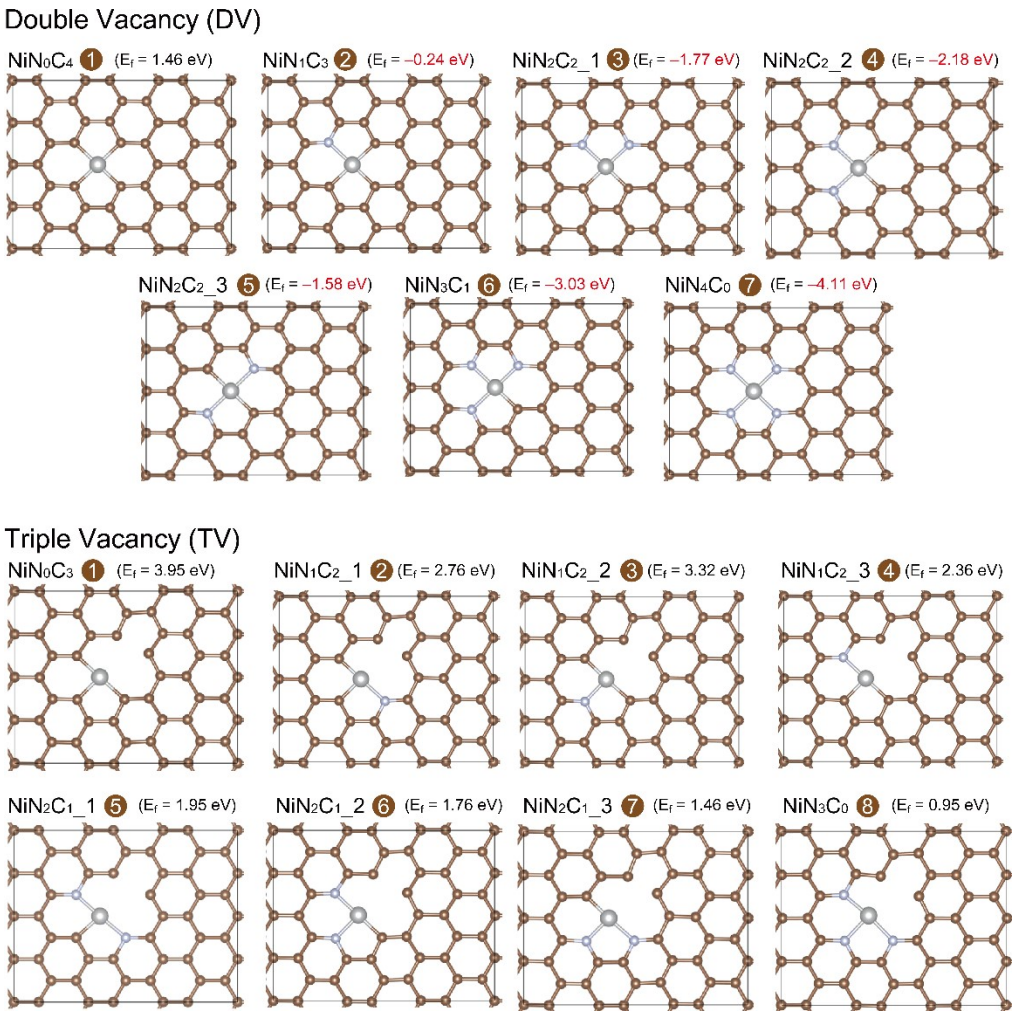

Fig. S31. Optimized structures Ni-SACs with double (DV) and triple vacancy (TV). For NiN_xC_y, x and y represent the number of N atoms and C atoms bonded to the Ni atom. For DV and TV, the Ni is coordinated to 4 sites and 3 sites on the graphene surface, respectively, hence the Ni-bonded C coordination number is 4-x and 3-x. NiN_xC_y_i (i=1, 2, and 3) represent a specific N decoration on the graphene surface with the same x and y. Certain configurations have a single configuration *i.e.*, one type of nitrogen decoration.

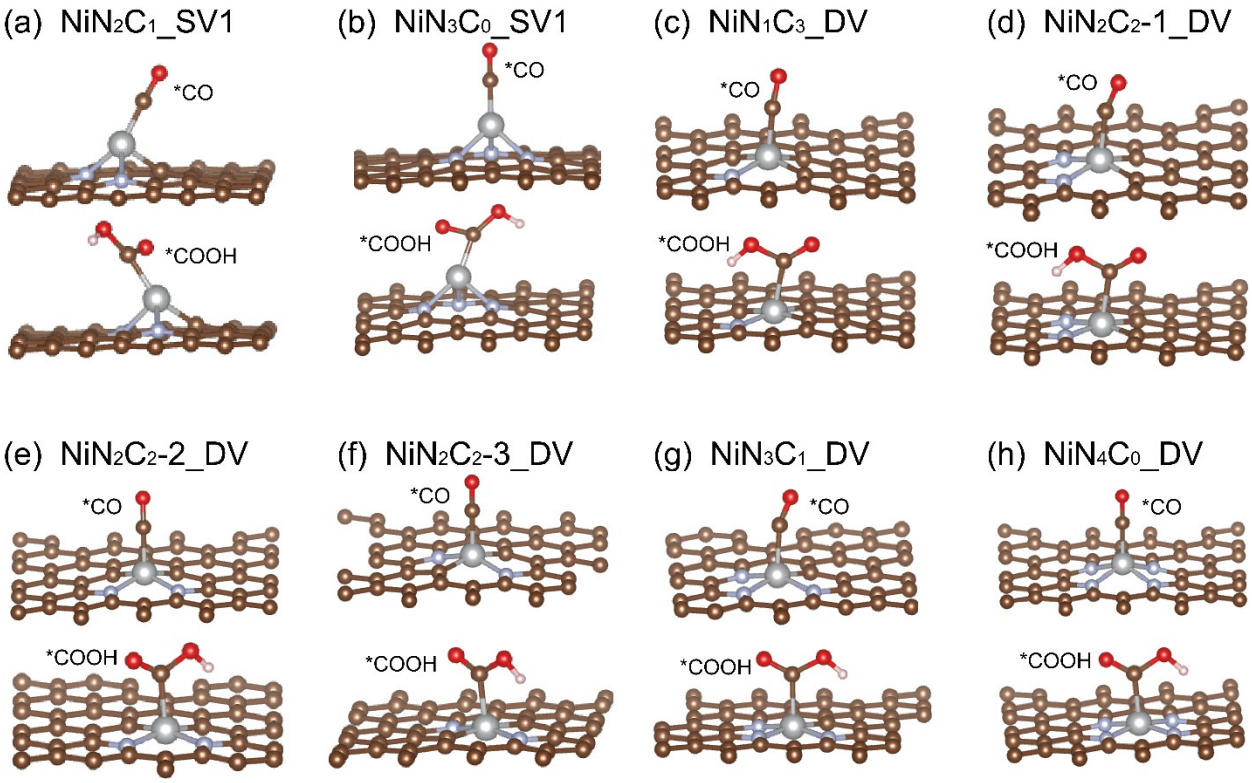

Fig. S32. The adsorbed *COOH and *CO configurations on the eight Ni-SACs with negative formation energy values in **Fig. 5**.

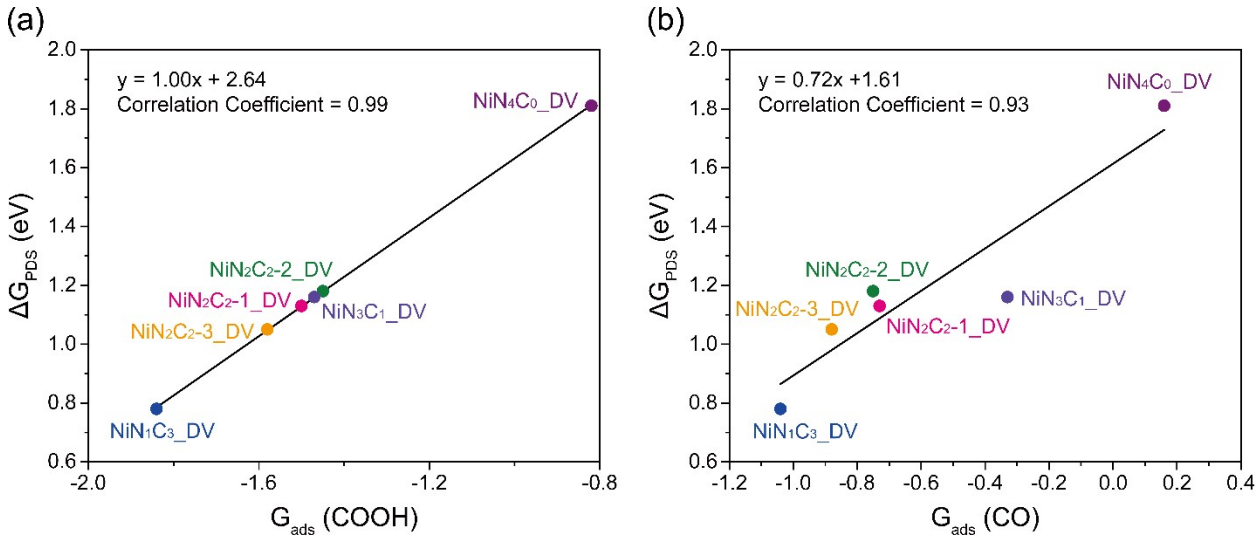

Fig. S33. The relationship between (a) G_{ads}(COOH) and ΔG_{PDS} and (b) G_{ads}(CO) and ΔG_{PDS}. A slope and intercept values along with the correlation coefficient of the linear relationship are provided in the inset.

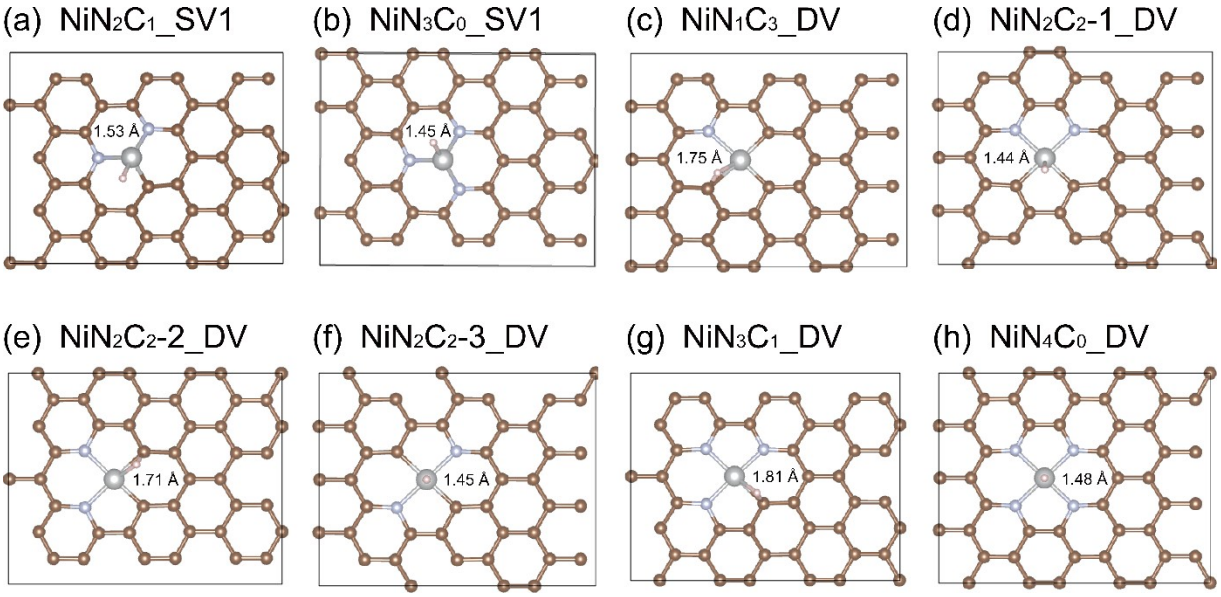

Fig. S34. The adsorbed *H configuration on the eight Ni-SACs.

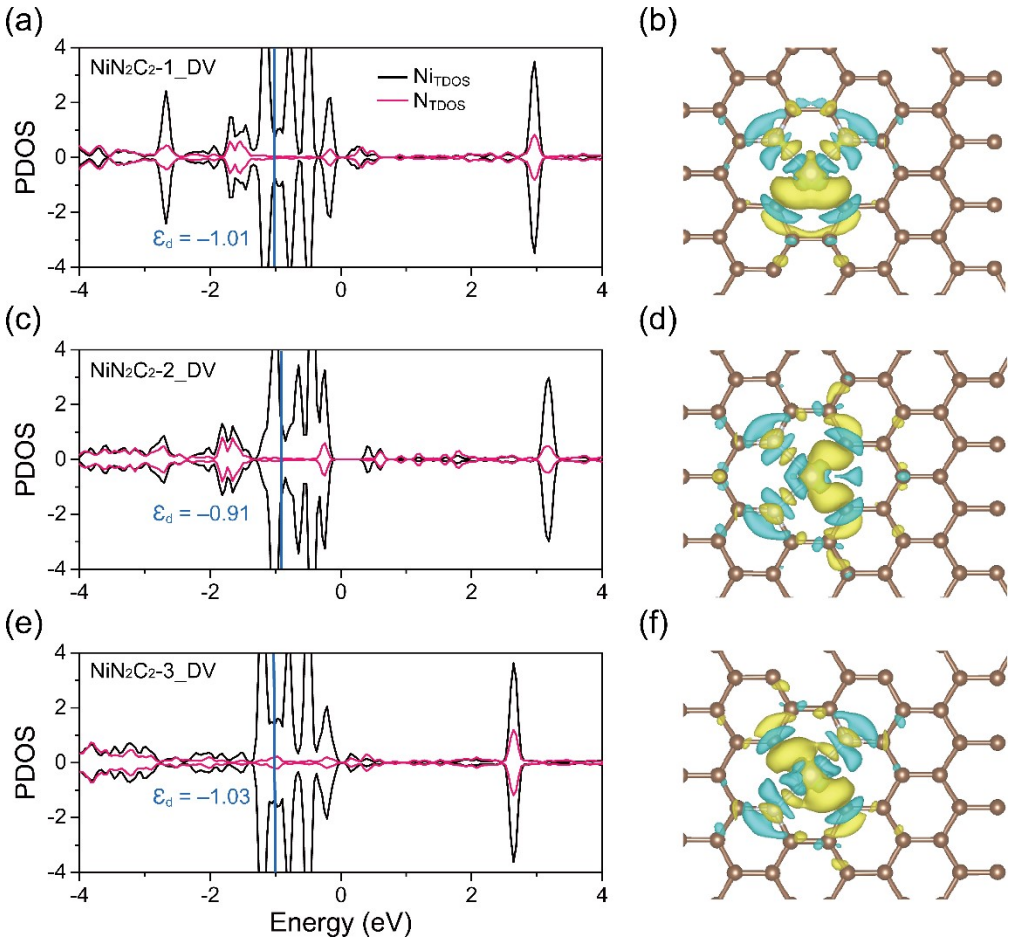

Fig. S35. (a, c, e) The projected density of states (PDOS) along with the d-band center of the 3 different rearrangements of NiN_2C_2_DV. (b, d, f) The charge density distribution around Ni single atom and N dopant, where blue and yellow regions represent charge depletion and accumulation.

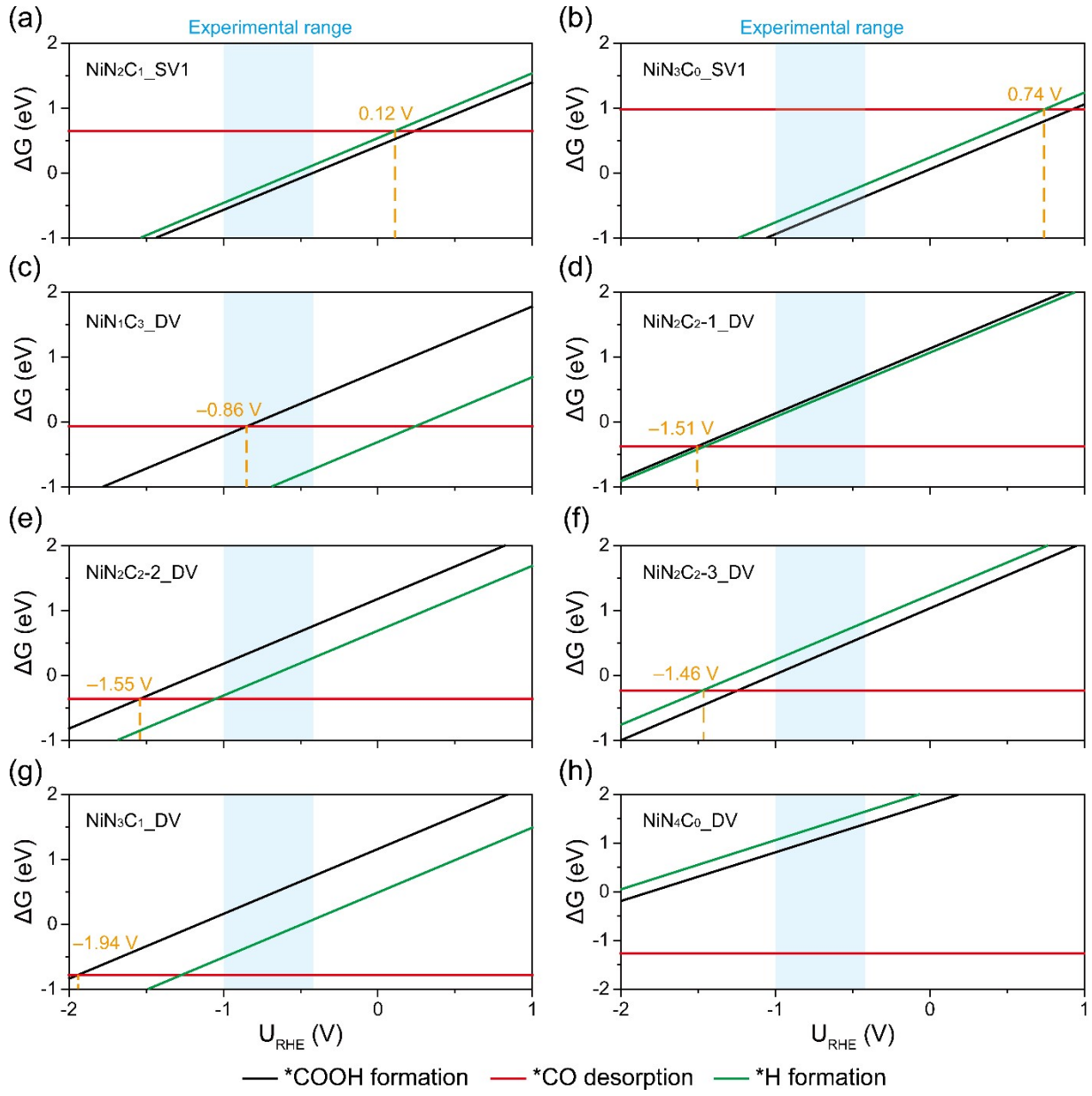

Fig. S36. The potential (U_{RHE}) dependent ΔG_U calculated for all *COOH formation (black line), *CO desorption (red line), and *H formation (green line) catalyzed by Ni-SACs. The experimental reductive potential range is marked on the top. The vertical dotted line (orange) represents the reductive potential beyond which CO poising is possible.

Table S1. Elemental analysis results and electrode specifications of Ni-SAC catalysts.

	ICP-OES (ppm)	**EA (wt%)**	**XPS (at%)**	**Mass loading[a] (mg cm_{geo}^{-2})**	
				Ni-SAC +Nafion	Ni-SAC
Ni-SAC -700/H_2	Ni: 29301.07	C: 68.2121 N: 17.8897 O: 4.4402 H: 1.3801	C: 80.16 N: 15.83 O: 3.43 Ni: 0.58	1.152(5)	0.401
Ni-SAC -800/Ar	Ni: 28219.79	C: 62.9856 N: 20.2528 O: 4.4519 H: 0.7755	C: 78.42 N: 18.30 O: 2.68 Ni: 0.60	1.153(7)	0.401
Ni-SAC -800/H_2	Ni: 38312.73	C: 74.3278 N: 12.0277 O: 3.4733 H: 0.8268	C: 86.29 N: 10.19 O: 2.69 Ni: 0.83	1.152(4)	0.401
Ni-SAC -900/Ar	Ni: 37081.86	C: 73.0521 N: 12.7101 O: 2.9833 H: 0.4563	C: 85.37 N: 11.58 O: 2.35 Ni: 0.70	1.151(3)	0.400
Ni-SAC -900/H_2	Ni: 54120.09	C: 78.1440 N: 8.0926 O: 1.8383 H: 0.4964	C: 90.1 N: 6.86 O: 2.38 Ni: 0.66	1.152(7)	0.401

[a] The areal loading of catalysts was determined by using at least 5 electrodes.

Table S2. Structural model for EXAFS fitting in this study.

Ni	Chemical formula	Ni
	Space group	$Fm\bar{3}m$
	Lattice constant	a = b = c = 3.47515 Å α, β, γ = 90°
	Atomic position	Ni (0, 0, 0)
Ni-Pc	Chemical formula	$C_{32}H_{16}NiN_8$
	Space group	$P2_1/c$
	Lattice constant	a = 14.489 Å, b = 4.763 Å, c = 19.156 Å α = 90°, β = 120.76°, γ = 90°
	Atomic position	Ni (0, 0, 0), N1 (0.2531, 0.0282, 0.1612), N2 (0.0732, 0.2194, 0.0973), N3 (–0.0713, 0.5227, 0.0786), N4 (–0.1313, 0.1968, –0.0331), C1 (0.1791, 0.1968, 0.1581), C2 (0.2018, 0.3964, 0.2227), C3 (0.2937, 0.4526, 0.2971), C4 (0.2858, 0.659, 0.3453), C5 (0.1902, 0.8051, 0.3203), C6 (0.0982, 0.7494, 0.2454), C7 (0.1064, 0.5414, 0.1976), C8 (0.0282, 0.4293, 0.1192), C9 (–0.1443, 0.4095, 0.0093), C10 (–0.2553, 0.5013, –0.0325), C11 (–0.3077, 0.7034, –0.0132), C12 (–0.4176, 0.7355, –0.0665) C13 (–0.4721, 0.5718, –0.1369), C14 (–0.4188, 0.3696, –0.1561), C15 (–0.3092, 0.339, –0.1025), C16 (–0.2297, 0.1511, –0.1022), H1 (0.3679, 0.339, 0.3168), H2 (0.3557, 0.7092, 0.4047), H3 (0.187, 0.9618, 0.359), H4 (0.0238, 0.8584, 0.2254), H5 (–0.2644, 0.8298, 0.0412), H6 (–0.4615, 0.8879, –0.0542), H7 (–0.5584, 0.6018, –0.178), H8 (–0.4616, 0.2439, –0.2109)

Table S3. The EXAFS fitting parameters and results for Ni-Pc.

Ni-Pc	Path	Model C.N.[a]	R_{model} (Å)	R_{fit} (Å)	ΔE (eV)	σ^2 ($\times10^{-3}$, Å^2)
Ni K-edge	Ni-N1	4	1.9151	1.88±0.01	1.684[b]	3±2
Structure model						
Lattice constant			a = 14.5, b = 4.8 Å, c = 19.2 Å			
Atomic position			Ni (0, 0, 0), N1 (0.869, 0.197, 0.967),			
Fitting results						
Independent points	4.2324219					
Number of variables	3					
Chi-square	27847.4786908					
Reduced chi-square	22595.7354829					
R-factor	0.0200521					
Number of data sets	1					
	Ni K-edge					
k-range	2.6 – 12.5					
***R*-range**	1.1 – 1.8					

[a] Amplitude reduction factor that made the coordination number of 4 for the Ni–N1 path in this data was further used for calculating the coordination of Ni species in the samples.

[b] This variable was fixed as the optimal value in the last fitting process step because of the uncertainty.

Table S4. The EXAFS fitting parameters and results for Ni-SAC-700/H_2.

	Path	Model C.N.	Fitted C.N.	R_{model} (Å)	R_{fit} (Å)	ΔE (eV)	σ^2 ($\times10^{-3}$, Å^2)
Ni K-edge	Ni-N1	4	3.5±0.2	1.9151	1.87±0.01	−1±2	8.95[a]
	Ni-C1	8	1.2±0.7	2.9455	2.68±0.04	−9.374[a]	6.05[a]
Fitting results							
Independent points			7.9218750				
Number of variables			5				
Chi-square			1900.1684561				
Reduced chi-square			650.3250331				
R-factor			0.0088145				
Number of data sets			1				
			Ni K-edge				
k-range			3.0 – 11.5				
***R*-range**			1.0 – 2.5				

[a] This variable was fixed as the optimal value in the last fitting process step because of the uncertainty.

Table S5. The EXAFS fitting parameters and results for Ni-SAC-800/Ar.

	Path	Model C.N.	Fitted C.N.	R_{model} (Å)	R_{fit} (Å)	ΔE (eV)	σ^2 ($\times10^{-3}$, Å^2)
Ni K-edge	Ni-N1	4	3.5±0.1	1.9151	1.868± 0.009	−3±1	10[a]
Fitting results							
Independent points	6.3085938						
Number of variables	3						
Chi-square	1125.0009762						
Reduced chi-square	340.0239078						
R-factor	0.0055604						
Number of data sets	1						
	Ni K-edge						
k-range	2.8 – 11.36						
***R*-range**	1.0 – 2.2						

[a] This variable was fixed as the optimal value in the last fitting process step because of the uncertainty.

Table S6. The EXAFS fitting parameters and results for Ni-SAC-800/H_2.

	Path	Model C.N.	Fitted C.N.	R_{model} (Å)	R_{fit} (Å)	ΔE (eV)	σ^2 ($\times10^{-3}$, Å^2)
Ni K-edge	Ni-N1	4	3.2±0.2	1.9151	1.87±0.02	−2±2	9.97[a]
Fitting results							
Independent points	5.3750000						
Number of variables	3						
Chi-square	3180.5579633						
Reduced chi-square	1339.1823003						
R-factor	0.0134865						
Number of data sets	1						
	Ni K-edge						
k-range	2.86 – 11.5						
***R*-range**	1.0 – 2.0						

[a] This variable was fixed as the optimal value in the last fitting process step because of the uncertainty.

Table S7. The EXAFS fitting parameters and results for Ni-SAC-900/Ar.

	Path	Model C.N.	Fitted C.N.	R_{model} (Å)	R_{fit} (Å)	ΔE (eV)	σ^2 ($\times10^{-3}$, Å^2)
Ni K-edge	Ni-N1	4	2.9±0.3	1.9151	1.872± 0.010	−2±1	10±2
Fitting results							
Independent points	6.0156250						
Number of variables	4						
Chi-square	503.5793262						
Reduced chi-square	249.8378052						
R-factor	0.0054667						
Number of data sets	1						
	Ni K-edge						
k-range	2.86 – 11.7						
***R*-range**	1.0 – 2.1						

Table S8. The EXAFS fitting parameters and results for Ni-SAC-900/H_2.

	Path	Model C.N.	Fitted C.N.	R_{model} (Å)	R_{fit} (Å)	ΔE (eV)	σ^2 ($\times10^{-3}$, Å^2)
Ni K-edge	Ni-N1	4	1.20± 0.07	1.9151	1.86±0.01	−2±2	8.41[a]
	Ni-Ni	12	4.38± 0.05	2.4573	2.487± 0.002	1.9±0.3	7.17[a]
Fitting results							
Independent points			9.9892578				
Number of variables			6				
Chi-square			257.4916939				
Reduced chi-square			64.5462655				
R-factor			0.0004427				
Number of data sets			1				
			Ni K-edge				
k-range			2.68 – 12.35				
***R*-range**			1.0 – 2.65				

[a] This variable was fixed as the optimal value in the last fitting process step because of the uncertainty.

Table S9. Bond length of Ni–N and Ni–C for the energetically optimized Ni-N_xC_y configurations.

		DFT-calculated bond length (Å)
NiN_2C_1_SV1	**Ni-N1**	1.87
	Ni-N2	1.87
	Ni-C1	1.82
NiN_3C_0_SV1	**Ni-N1**	1.89
	Ni-N2	1.88
	Ni-N3	1.88
NiN_1C_3_DV	**Ni-N1**	1.93
	Ni-C1	1.88
	Ni-C2	1.86
	Ni-C3	1.86
NiN_2C_2-1_DV	**Ni-N1**	1.94
	Ni-N2	1.95
	Ni-C1	1.83
	Ni-C2	1.83
NiN_2C_2-2_DV	**Ni-N1**	1.94
	Ni-N2	1.94
	Ni-C1	1.83
	Ni-C2	1.83
NiN_2C_2-3_DV	**Ni-N1**	1.89
	Ni-N2	1.89
	Ni-C1	1.87
	Ni-C2	1.87
NiN_3C_1_DV	**Ni-N1**	1.91
	Ni-N2	1.92
	Ni-N3	1.87
	Ni-C1	1.85
NiN_4C_0_DV	**Ni-N1**	1.88
	Ni-N2	1.88
	Ni-N3	1.88
	Ni-N4	1.88

Table S10. Bader charge analysis of Ni-SACs with different vacancy and N decoration. The charge depletion on the Ni atoms is presented as Ni(+q).

Vacancy types	Entry	Ni(+q)
SV1	NiN_2C_1	0.71
	NiN_3C_0	0.8
SV2	NiN_1C_4	0.68
	NiN_2C_2-1	0.69
	NiN_2C_2-2	0.66
	NiN_2C_3-3	0.71
	NiN_3C_1	0.74
	NiN_4C_0	0.80

Table S11. The limiting potential (U_{PDS}, in V) values calculated from the PDS of CO_2RR and HER processes and the difference (ΔU_{PDS}) between the U_{PDS} values for both processes.

	U_{PDS} [CO_2RR]	U_{PDS} [HER]	U_{PDS} [CO_2RR] – U_{PDS} [HER]
NiN_2C_1_SV1	-0.65	-0.54	-0.11
NiN_3C_0_SV1	-0.96	-0.24	-0.72
NiN_1C_3_DV	-0.78	-0.31	-0.47
NiN_2C_2-1_DV	-1.13	-1.06	-0.06
NiN_2C_2-2_DV	-1.18	-0.69	-0.49
NiN_2C_2-3_DV	-1.05	-1.24	0.19
NiN_3C_1_DV	-1.16	-0.49	-0.67
NiN_4C_0_DV	-1.81	-2.07	0.26

Table S12. Bond length of Ni–N and Ni–C before and after intermediates adsorption.

		Before adsorption	After adsorption		
			***COOH**	***CO**	***H**
NiN_2C_2-1_DV	**Ni-N1**	1.94 Å	1.95 Å	1.99 Å	1.92 Å
	Ni-N2	1.95 Å	1.96 Å	1.99 Å	1.91 Å
	Ni-C1	1.83 Å	1.85 Å	1.88 Å	1.91 Å
	Ni-C2	1.83 Å	1.86 Å	1.88 Å	1.87 Å
	∠C-C-N-Ni	0.03°	7.89°	14.25°	5.59°
NiN_2C_2-3_DV	**Ni-N1**	1.89 Å	1.91 Å	1.96 Å	1.90 Å
	Ni-N2	1.89 Å	1.92 Å	1.96 Å	1.90 Å
	Ni-C1	1.87 Å	1.88 Å	1.90 Å	1.87 Å
	Ni-C2	1.87 Å	1.88 Å	1.90 Å	1.87 Å
	∠C-C-N-Ni	0.01°	13.74°	17.89°	7.31°

Table S13. The d-band center (ε_d) and free energy change of *COOH and *H formation on NiN_2C_2-1_DV, NiN_2C_2-2_DV, and NiN_2C_2-3_DV.

	ε_d	ΔG_{*COOH}	ΔG_{*H}
NiN_2C_2-1_DV	-1.01	1.13	1.06
NiN_2C_2-2_DV	-0.91	1.18	0.69
NiN_2C_2-3_DV	-1.03	1.05	1.24